Mesoscale eddies, coastal upwelling, and the upper-ocean heat budget in the Arabian Sea

Albert S. Fischer[a],*, Robert A. Weller[a], Daniel L. Rudnick[b], Charles C. Eriksen[c], Craig M. Lee[d], Kenneth H. Brink[a], Chad A. Fox[e], Robert R. Leben[e]

[a] *Department of Physical Oceanography, MS 29 Woods Hole Oceanographic Institution, Woods Hole, MA 02543, USA*
[b] *Scripps Institution of Oceanography, University of California, San Diego, La Jolla, CA 92093-0230, USA*
[c] *School of Oceanography, University of Washington, Seattle, WA 98195, USA*
[d] *Applied Physics Laboratory, University of Washington, Seattle, WA 98185, USA*
[e] *Colorado Center for Astrodynamics Research, University of Colorado, Boulder, CO 80309, USA*

Abstract

Estimation of the terms in the upper-ocean heat budget from a moored array in the central Arabian Sea shows periods when a rough balance between the temperature trend and the horizontal advection of heat exists. Altimetry and sea-surface temperature imagery are used to demonstrate that these episodes of strong horizontal advection are associated with mesoscale features. During the wintertime Northeast (NE) Monsoon these are capped-off mesoscale eddy features generated during the previous summertime Southwest (SW) Monsoon and have little horizontal transport of heat within the mixed layer. During the SW Monsoon the major contribution is strong offshore export of coastally upwelled water in a filament with a strong surface presence. Temperature and salinity properties from the moored array and a SeaSoar survey during the formation of the coastal filament confirm the offshore transport of the upwelled water mass to the site of the moored array, more than 600 km offshore. Estimates of the filament section heat flux are several percent of the total estimated heat flux due to upwelling along the Arabian Peninsula, and remote sensing data show that similar mesoscale variability along the coast is enhanced during the SW Monsoon. This points to the importance of mesoscale-modulated transports in not only the observed heat budget at the moored array, but in the overall upper-ocean heat budget in the Arabian Sea. © 2002 Elsevier Science Ltd. All rights reserved.

1. Introduction

The Arabian Sea is a unique environment for studying the forced upper-ocean response, with strong and distinct atmospheric forcing regimes, and a clear separation in the time domain between mesoscale oceanic variability and variability in the atmospheric forcing. It is influenced by a unique monsoonal cycle, with reversing wind forcing, an evaporative fresh-water flux over most of the basin, and an annual mean heat gain. The wintertime Northeast (NE) Monsoon is characterized by mild to moderate wind stress and an oceanic heat loss leading to a destabilizing surface

*Corresponding author. Laboratoire d'Océanographie Dynamique et de Climatologie, 4 place Jussieu—boîte 100, 75252 Paris Cedex 05, France. Fax: +33-1-4427-7159.
E-mail address: albert.fischer@lodyc.jussieu.fr (A.S. Fischer).

buoyancy flux for the ocean. The summertime Southwest (SW) Monsoon brings strong surface wind forcing across the central Arabian Sea in the form of the Findlater Jet (Findlater, 1969), and a neutral to strongly stabilizing surface-buoyancy flux. The two intermonsoon seasons are characterized by weak wind forcing and large evaporative and heat fluxes.

The marked seasonal cycle in the surface forcing over the Arabian Sea leads to a strong seasonal cycle in the circulations of the western Arabian Sea. Chief among these is the annual reversal of the Somali Current on the basin's western boundary (e.g., Schott, 1983), with peak currents up to $3.7 \, \text{m s}^{-1}$ during the SW Monsoon. Observations also have found a vigorous mesoscale eddy field in the Arabian Sea (Molinari et al., 1990; Flagg and Kim, 1998; Kim et al., 2001). The SW Monsoon wind field causes upwelling along the Arabian coast, leading to observed persistent jets of cold upwelled water extending from the Omani coast, often reaching hundreds of kilometers into the interior (Brink et al., 1998).

A striking feature of the upper ocean is the deepening and cooling of the mixed layer in the central northwestern Arabian Sea during both the SW and NE Monsoon seasons (Rao et al., 1989). A canonical explanation for the deepening and observed gradients in mixed-layer depth during the SW Monsoon is given by Bauer et al. (1991), who propose that shoreward of the Findlater Jet open-ocean upwelling pulls the thermocline closer to the surface, yielding shallower mixed layers, while on the offshore side wind-stress-curl-driven downwelling deepens the mixed layers. More recently Lee et al. (2000) have shown that variations in turbulent wind-driven entrainment are more likely to be the cause of this gradient in mixed-layer depth, though this cannot fully explain the observed mixed-layer depth patterns, which are also likely influenced strongly by horizontal advection (Rao et al., 1989). Recent moored observations (see Weller et al., 2002) found that the deepening and cooling of the mixed layer was locally forced during the NE Monsoon primarily by the negative surface heat flux, and during the SW Monsoon by the wind stress.

Outside of the regions of coastal upwelling during the SW Monsoon, sea-surface temperatures (SSTs) are generally quite high (averaging between 27°C and 29°C), and thus even small variations in temperature may produce significant impacts on the atmospheric circulation (Palmer and Mansfield, 1984). The links between the Arabian Sea SST and the strength of the monsoon circulation remain unclear—Shukla (1987) found a correlation between heavy monsoon rainfall and subsequent negative SST anomalies, while Rao and Goswami (1988) found warmer SSTs during the Spring Intermonsoon significantly correlated with heavier rainfall during the SW Monsoon. The net annual heat input into the ocean over the Arabian Sea also must be carried southward by the ocean circulation, and forms an important part of the total combined atmospheric–oceanic meridional heat transport in the Indian Ocean sector (Hastenrath and Greischar, 1993), both on the seasonal and the annual mean time scales.

The upper-ocean heat budget and ultimately the SST are influenced by numerous factors, among them solar heating, surface heat losses, turbulent and convective entrainment, horizontal heat flux divergences (advection), and vertical advection induced by Ekman pumping or associated with mesoscale flows. A number of models have successfully treated the mixed layer as being governed by one-dimensional processes (Price et al., 1986; Large et al., 1994), ignoring horizontal and vertical advection. But in a region of strong oceanic gradients Rudnick and Weller (1993) found that the horizontal advection of heat was the dominant term in the upper-ocean heat balance. The horizontally advective terms also have been found to be important in the western Pacific Ocean's warm-pool region (Feng et al., 1998), and in the eastern North Atlantic Ocean's subduction region, Spall et al. (2000) found both horizontal and vertical advection important in the annual mean heat budget of the upper ocean.

During the ONR-sponsored Forced Upper Ocean Dynamics program, conducted in coordination with the US JGOFS Arabian Sea Process Study (Smith et al., 1998), an effort was made to assess the relative contributions of these various processes. A moored array of surface

and subsurface moorings sampled the upper ocean from October 1994 to October 1995, covering a full monsoonal cycle. The array measured the evolution of vertical structure at four sites and allowed estimations of the surface forcing from surface meteorology (see Weller et al., 1998), oceanic horizontal gradients and velocities, and thus advective fluxes.

The following section describes the methods and data used in the paper, which include the estimation of terms in the upper-ocean heat budget from data in the moored array, and then the use of sea-surface altimetry, satellite sea-surface temperature, and SeaSoar estimates of upper-ocean volume data to build our understanding of the physical processes responsible for the dominant terms. The combination of these three types of data—the moored array, remotely sensed from satellites, and the SeaSoar surveys—yields an integrated picture, impossible to form with any one type of data alone, and demonstrates the importance of mesoscale-modulated transports in the heat budget of the Arabian Sea.

2. Methods and data

2.1. Heat budget and the Arabian Sea moored array

The data from the moored array are used to estimate the terms of the equation of the conservation of heat,

$$\rho_0 C_p \left[\frac{\partial T}{\partial t} + \mathbf{u} \cdot \nabla T + w \frac{\partial T}{\partial z} \right] = \frac{\partial}{\partial z}(q - r), \quad (1)$$

where T is the temperature, t is time, $\mathbf{u}$ is the vector horizontal velocity, ∇ is the horizontal gradient operator, w is the vertical velocity, z is the vertical coordinate (positive upwards), q is the penetrating solar heat flux, r is the turbulent heat flux, ρ_0 is a reference density (assumed constant at $1025 \, \text{kg} \, \text{m}^{-3}$), and C_p the specific heat capacity of seawater (assumed constant at $3994 \, \text{J} \, \text{kg}^{-1} \, {}^{\circ}\text{C}^{-1}$). The trends in heat ($\rho_0 C_p T$), plus horizontal and vertical advection of heat, are balanced by the vertical divergence of solar and turbulent heat fluxes.

Turbulent fluxes were not measured at the moored array, so after examination of the vertically resolved horizontal heat flux, the terms in the vertically integrated conservation of heat are estimated:

$$\rho_0 C_p \left[\int_{-h}^0 \frac{\partial T}{\partial t} \mathrm{d}z + \int_{-h}^0 \mathbf{u} \cdot \nabla T \, \mathrm{d}z + \int_{-h}^0 w \frac{\mathrm{d}T}{\mathrm{d}t} \right]$$
$$= Q_0, \quad (2)$$

where the depth $-h$ is assumed to be below the depth of turbulent fluxes. The first term on the left-hand side is the temperature trend (which is estimated from the observed changes in temperature), the second the horizontal advection of heat (estimated from the velocity and temperature gradients across the array), and the third term is the vertical advection of heat, which is a residual term since the vertical velocity is not directly measured. The right-hand side, Q_0, is the surface heat flux (measured at the central element of the array). The vertical integration below the depth of turbulent penetration has eliminated the turbulent flux divergence. Limited by the lack of instruments at greater depth, the depth $-h$ is here always $125 \, \text{m}$, which is well below the maximum depth of the temperature-defined mixed layer (about $100 \, \text{m}$ during the NE Monsoon). The heat budget does not separate entrainment into the mixed layer. Each of the terms in (2) has units of $\text{W} \, \text{m}^{-2}$.

The location of the moored observations, centered at $15.5°\text{N}$, $61.5°\text{E}$, was selected for its proximity to the climatological axis of the atmospheric Findlater Jet, sampling the strongest surface forcing, and its distance from the complicating effects of the coast (see Fig. 1). Five moorings were deployed in a square approximately $55 \, \text{km}$ on each side in $4020 \, \text{m}$ water depth, from October 1994 to October 1995. Surface meteorological and subsurface oceanographic instrumentation on the moorings yielded the first concurrent, high-quality record of near-surface atmospheric forcing and upper-ocean response over the full monsoonal cycle (Weller et al., 1998). The moorings making up the array had two deployments, the first from October through April, covering the NE Monsoon and the Spring Intermonsoon, and the second from April through
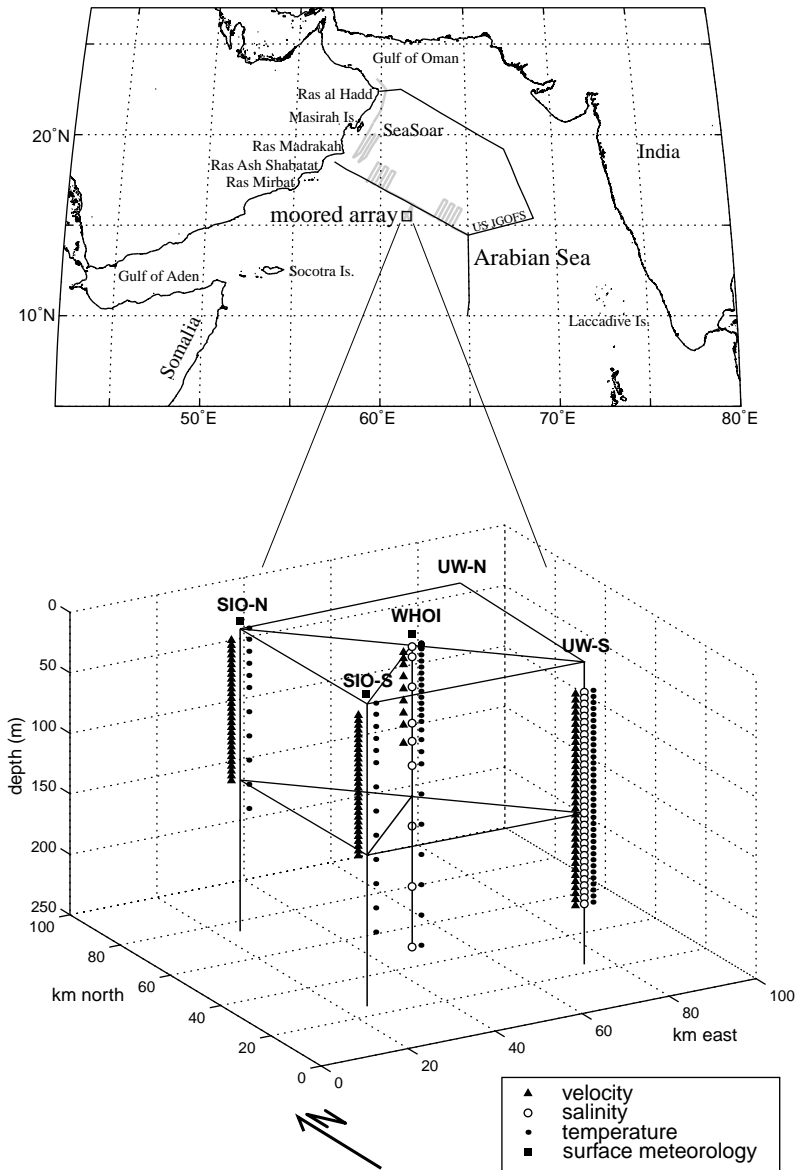
Fig. 1. The Arabian Sea Upper Ocean Dynamics moored array, centered at 15.5°N, 61.5°E. Five elements (four which returned data) formed a square of about 55 km per side in the north central Arabian Sea. On the map, above, the thin black line marks the cruise track of the US JGOFS Process Study, while the thick grey line marks the SW Monsoon SeaSoar survey track.

October, with newly calibrated sensors in place for the SW Monsoon and the shorter Fall Intermonsoon.

The two eastern elements, UW-N and UW-S, were moorings with subsurface profiling current meters (PCMs, deployed by C. Eriksen, UW)

measuring a profile of currents, temperature and salinity between 20 and 200 m every 4 h. The northern PCM mooring UW-N parted and the instrument was lost. The two western elements (deployed by D. Rudnick, SIO) were surface toroid buoys, SIO-N and SIO-S, each of which

supported a downward-looking acoustic Doppler current profiler (ADCP) and a series of temperature recorders spaced along the mooring line. The central element WHOI was a surface discus buoy (deployed by R. Weller, WHOI), which supported a series of instruments measuring temperature, salinity, and currents. The surface moorings were instrumented with basic meteorological sensors, and the central mooring additionally with measurements of the incoming shortwave and longwave radiation. The central mooring surface meteorological data were used to estimate the surface heat flux for the array.

The spacing of the elements was designed to resolve the typical horizontal variability in the ocean based on satellite imagery and the local Rossby radius of deformation (the first baroclinic mode deformation radius is 64 km, based on a CTD cast at the site of the central mooring). A pre-deployment XBT survey of the area surrounding the array site found horizontal variations on the order of $1.0–1.5°C$ in the thermocline (much reduced near-surface), with scales much larger than the spacing of the array elements. Estimates of the horizontal decorrelation length scale of temperature from four SeaSoar surveys (Lee et al., 2000) varied from 25 to 100 km depending on the time of year and distance offshore. Horizontal variability on the small end of these estimates, not resolved by the array, may be a source of unaccounted error in the calculation.

All four elements of the array returned data in temperature and velocity for the first deployment (October 1994–April 1995), while during the second deployment, the triangle formed by the three moorings SIO-S, WHOI, and UW-S was used in the calculation due to a $<50\%$ data return in temperature on SIO-N. However, the near-surface temperature gradient during the second deployment was estimated including data from SIO-N. The data included in the calculation were averaged to 4 h, the time-base of the UW-S PCM profiles.

The terms in the conservation of heat equation were estimated for the central point of the four (three) moorings used in the first (second) deployment. Since the moored measurements contain variability on all scales, an EOF-filtering technique

was used to extract variability coherent across the array. The horizontal gradient in temperature was estimated from the moored point measurements using plane fits. The EOF filter also allowed an estimation of the uncertainties in the measurements, which propagated through the calculation, and are detailed in the Appendix A.

2.2. Remote sensing data

The moored array allows a detailed estimation of the terms in the heat budget at one point in the Arabian Sea. Two forms of remotely sensed data, altimetry and satellite sea-surface temperature, set the context for the surface flows and yield insights into the mesoscale dynamics responsible for major contributions to the heat budget.

2.2.1. Altimetry

To maximize the information about surface geostrophic flows associated with mesoscale features, a combined TOPEX/ERS altimetry product was used, which takes advantage of the high track resolution of the ERS altimeters, and the higher temporal resolution of the TOPEX/Poseidon altimeter (Fox, 1997). The TOPEX/Poseidon altimeter has an orbit with an exact repeat period of ten days, and a nominal track spacing in the Arabian Sea of about 250 km. For the period investigated, ERS-1 started in a 168-day exact repeat with 17-day near repeat orbit. On 21 March 1995 this changed to a 35-day exact repeat orbit, with a nominal track spacing in the Arabian Sea of about 80 km. The ERS-2 altimeter flew in a 35-day exact repeat orbit starting 21 April 1995, with the same nominal track spacing of 80 km.

Standard error corrections to the altimetry were applied before the two products were combined, detailed in Fox (1997). Additional corrections included an improved tidal model (Desai and Wahr, 1995) for the TOPEX altimetry. The TOPEX and ERS data were then blended and gridded using an optimal interpolation method. First, orbit and other environmental errors were removed from both the TOPEX and ERS data using along-track loess filtering, removing a running least squares fit of a tilt and bias within a sliding window. The window width was

approximately 15° in latitude, retaining mesoscale signals, but eliminating larger-scale sea-surface height (SSH) variations, including large-scale steric height variations. The data from the two altimeters were then combined and interpolated onto a 0.25° grid using a multi-grid preconditioned Cressman analysis (Hendricks et al., 1996). Interpolated maps were generated every three days, with TOPEX data within ± 10 and ERS data within ± 17 days used in the analysis. The final decorrelation radius used was 100 km.

A comparison of the combined altimetry product with the record from the mooring shows that it accurately captured the mesoscale variability seen at the moored array. To compare heights directly, the dynamic height anomaly at the WHOI mooring was calculated using 36-h smoothed data over the upper 250 m. If there is no motion at the lower limit of integration, the dynamic height is equivalent to the height of the sea surface. No direct measurements of velocity at 250 m are available, but the velocities at 300 m were much reduced compared to the surface velocities, by an order of magnitude (Weller et al., 2002). The correlation between dynamic height at the mooring and the altimeter height is good at 0.85 (see Fig. 2), and the rms difference between the demeaned time-series is 3.4 cm, comparable to the differences seen between altimetric and tide gauge measurements of sea level (4.3 cm, Mitchum, 1994). In particular, the timing of major changes in the sea-surface height in November and December 1994 and in August 1995 were well represented. The sharpness of the changes in the moored record was not reproduced in the altimetry, but these differences could be accounted for by smoothing and the removal of the long-wavelength signal in the altimetric mapping method. The surface velocities also compare reasonably well. Fig. 3 shows the 5-m velocity record from the WHOI mooring as 72-h means, along with the geostrophic velocity anomaly for the same point from the altimeter record calculated using a centered difference. While the major currents—including the sweep from a southeastward to northwestward current in November and December 1994 and the change from a strong northeastward to southeastward current in July and August of 1995—are reproduced, there are differences between the two, and the correlation is 0.68. The differentiation required to pass from SSH to velocity acts as a highpass filter, increasing the relative level of error, so the lower correlation is not unexpected. In addition, errors in the geoid on the grid scale will manifest themselves as persistent errors in the velocity and may contribute to the mismatch. The observed velocities also could be associated with density fields too small to be resolved in the altimetry, and include a small component of directly wind-driven velocity.

2.2.2. Sea-surface temperature imagery

Satellite-derived sea-surface temperature supplemented data from the altimeter. The data used
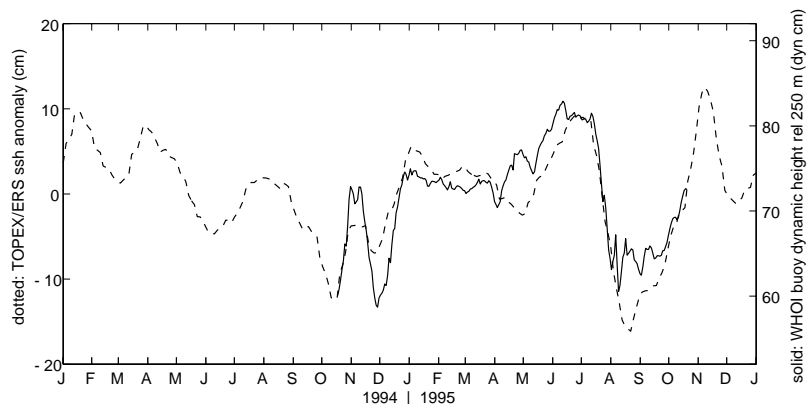

Fig. 2. Comparison of TOPEX/ERS altimetry SSH anomaly (*dashed*, every 3 days) and WHOI mooring-derived dynamic height (*solid*, 36-h smoothed), The correlation between the two time-series is 0.85.
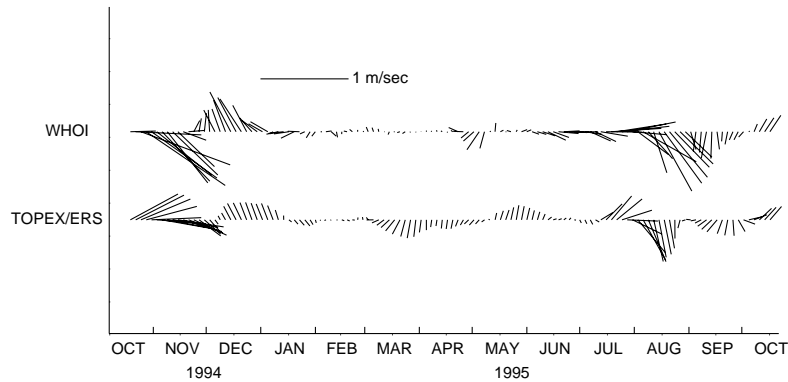
Fig. 3. Comparison of the surface velocity from the moorings (WHOI 5 m) and derived surface geostrophic velocity anomaly from the TOPEX/ERS altimetry. Correlation is 0.68.

here come from the NOAA/NASA advanced very-high resolution radiometer (AVHRR) pathfinder SST product (Kilpatrick et al., 2001). The imagery analyzed is the "best SST" Pathfinder product, which discards poor-quality data, generally those with clouds and near the edges of a swath. The nominal resolution of the data is 9 km. To match the time-base of the altimetry, daily retrievals of the SST are composited into 3-day bins centered on the same time-base as the altimetry, although on occasion this is extended to 7- or 9-day bins to overcome cloudiness. Only night-time passes are used, when the skin temperature measured by the AVHRR is presumably more representative of the 'bulk' mixed-layer temperature as convection is active. During the daytime, gradients in tempera-ture tend to be masked by the thin mixed layer that forms in response to diurnal heating. The analyzed temporal sequences were chosen as a balance between even time resolution and cloudiness, which was a particular problem during the SW Monsoon.

Overlaid SSH and SST generally show excellent correspondence. For example, at the end of the 1994 SW Monsoon (see Fig. 11a) the contours of the altimetry clearly show the upwelling wedge and retroflection of the Somali Current in the Great Whirl, as well as structure extending to the northeast towards the (future) site of the moored array. This structure in the sea-surface height is echoed in the sea-surface temperature. The data as a whole also confirm that the north–central

Arabian Sea has high levels of mesoscale varia-bility, particularly in the regions north and west of the moored array, intensified in large regions during the SW Monsoon and the following Fall Intermonsoon.

2.3. Seasoar data

Complementing the detailed point-wise view of the moored array and the broad-scale surface view provided by the altimetry and SST imagery, a SeaSoar survey during the SW Monsoon of a mesoscale filament feature provided a 'snapshot' view of a coastal upwelling filament which was a major contributor to the SW Monsoon array's heat budget. SeaSoar is an undulating, towed platform containing conductivity, temperature, and pressure sensors, as well as bio-optical sensors. It is typically towed between 1 and 300 m, with 3-km horizontal resolution along-track. Four cruises were undertaken during 1994–1995 (Lee et al., 2000), mapping the southern US JGOFS line, intensively surveying two 'radiator' patterns inshore and offshore of the moored array position, and making one 'butterfly' pattern around the moored array. Alerted by AVHRR imagery, the SW Monsoon survey (20 June—3 July 1995) also included a filament radiator survey near the coast between Ras Madrakah and Masirah Island (see Fig. 1). A shipboard acoustic Doppler current profiler (ADCP) concurrently measured currents in the upper ocean. A two-dimensional objective

mapping method at fixed depth levels created a three-dimensional gridded snapshot of the upper ocean in each of these radiator patterns, which took about 2.5 days to sample. The internal tide, diurnal variations, and near-inertial motions are thus aliased into the data for each survey, but are not large enough to obscure mesoscale features and the geostrophic flow.

3. Results and discussion

3.1. Heat budget

The net surface heat flux at the moored array has a strong diurnal cycle, though its daily mean varies on synoptic to seasonal time-scales (Fig. 4).

During the NE Monsoon, it was generally negative, with the ocean losing heat. During the Intermonsoon seasons it was strongly positive, and generally positive during the SW Monsoon, except during the few days when the wind stress reached its maximum. Estimation of the one-dimensional heat balance using the central mooring in the array (see Weller et al., 2002, reproduced in Fig. 4, bottom) suggests a reasonable balance between the input of heat through the surface heat flux and the oceanic heat gain for certain periods of the year, when the oceanic heat gain was integrated from the surface to below a depth where losses from turbulent fluxes are thought to be important. These windows include the end of the NE Monsoon through the Spring Intermonsoon, and the end of the SW Monsoon through the Fall
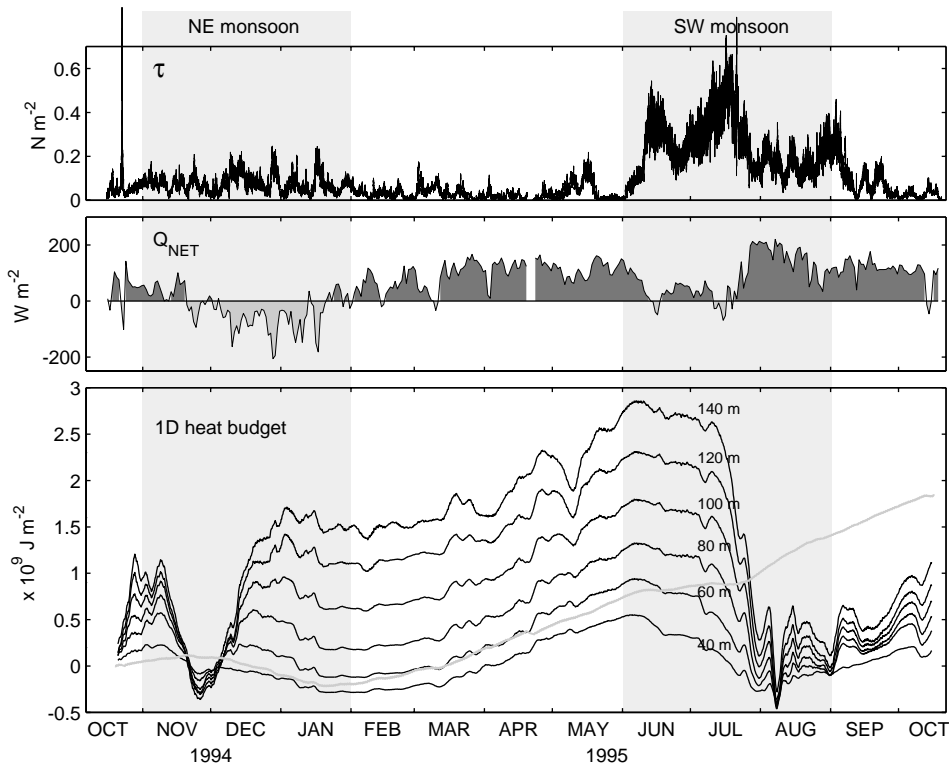

Fig. 4. The surface wind stress (τ), surface net heat flux (Q_{NET}), and the one-dimensional balance between heat in the ocean, integrated to a fixed depth (*thin black lines*) and the heat transferred by the surface heat flux (*thick grey line*). When the slopes of each match, the oceanic heat gain is roughly in balance with the net surface heat flux. This occurs at the end of the NE Monsoon and through the Spring Intermonsoon, and roughly, at the tail end of the SW Monsoon and into the Fall Intermonsoon. The periods of major departure from this 1-D balance are during the early NE Monsoon (October–early December) and the SW Monsoon (June and July).

Intermonsoon. There were some major departures from this balance, notably in November–December and in June–July. During these periods, the heat content of the upper ocean changed rapidly owing to a process other than the surface heat flux.

There was a twice-yearly cycle of sea-surface temperature and mixed-layer response to the surface forcing evident in the array's average temperature (Fig. 5). The mixed layer deepened in response to convective cooling during the NE Monsoon, while the SST cooled under the effect of the resulting entrainment as well as the surface cooling. The mixed layer shoaled with restratification and an SST rise during the Spring Intermonsoon. The stronger winds of the SW Monsoon again brought mixed-layer deepening and cooling. Below the influence of the surface forcing, however, the thermocline depth varied considerably during the year. The 21°C isotherm for example, which was never incorporated into the mixed layer and represented the upper thermocline, varied in depth from a minimum of about 60 m at the beginning of the NE Monsoon to 120 m for the rest of the NE Monsoon and into the SW Monsoon. It shoaled suddenly at the end of July, coincident with a sharp reduction in SST and a shoaling of the mixed layer. The temporal change in temperature at a fixed depth at the array below the influence of surface fluxes, over the course of the year (a range of 7.7°C at 100 m), was as large or larger than the change in the SST (6.0°C near the surface).

The periods when the one-dimensional balance failed in the temperature field over the array were mirrored in the array's velocity field (Fig. 6). The strongest velocities of the year came during
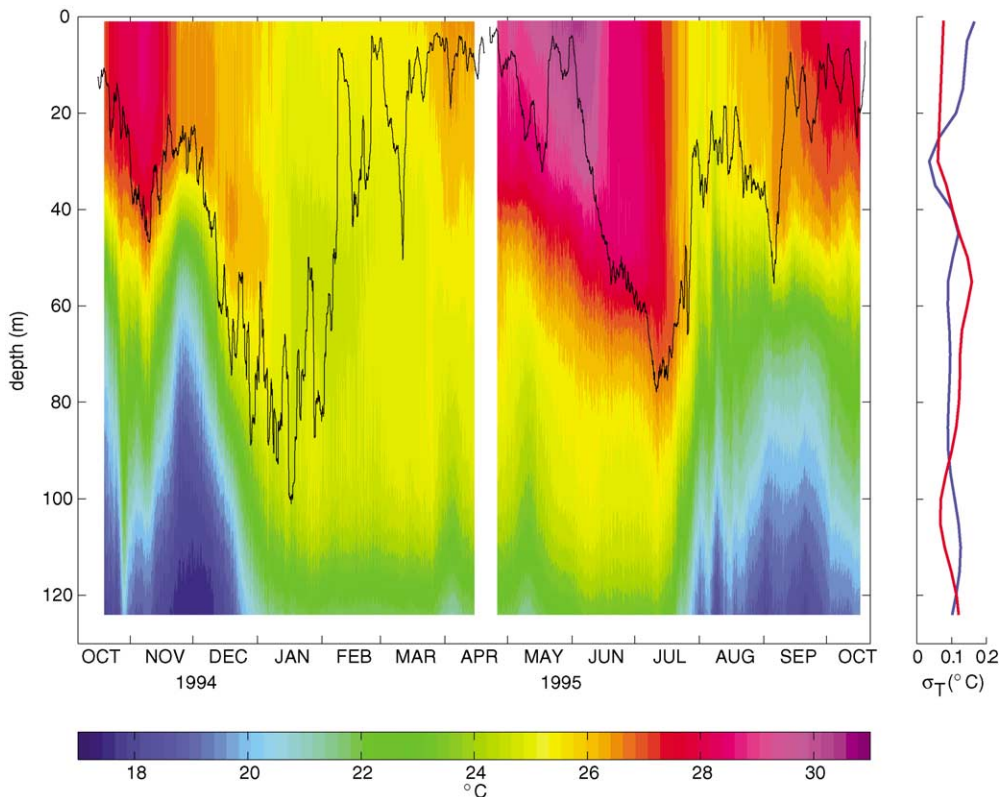

Fig. 5. The array average temperature is shown in the main panel, while the uncertainty due to the EOF filtering is shown at right, blue for the first deployment and red for the second. The uncertainty is generally around 0.1°C though it varies in depth. The daily mean mixed-layer depth (*black*) is shown as recorded at the WHOI mooring, from a 0.1°C difference from SST criterion.
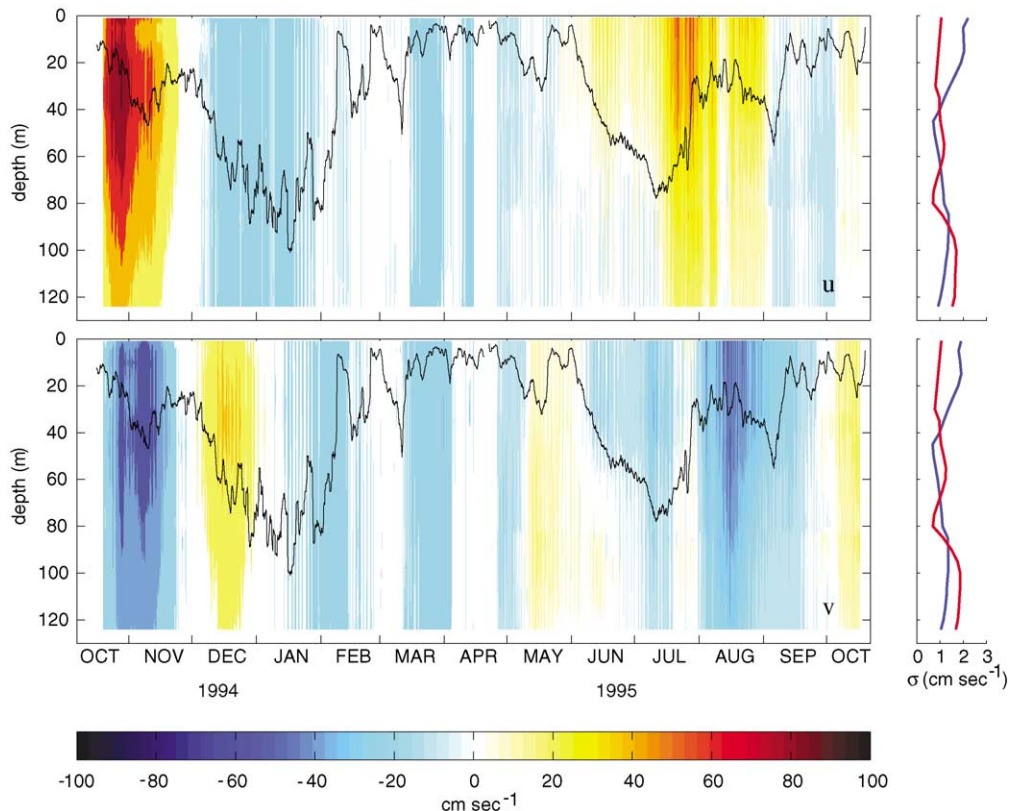
Fig. 6. The array average east (u, *top*) and north (v, *bottom*) components of the velocity. Error due to EOF filtering is shown at right, blue for the first deployment and red for the second. The daily average (*black*) mixed-layer depths recorded at the WHOI mooring are shown.

the beginning of the NE Monsoon, beginning with a strong southeastward velocity which turned northeastward through December. Another strong signal was the east and southeastward velocity in July and August. These were coincident with the strong thermocline depth changes already noted. The velocities, though surface-intensified, were fairly constant across the mixed layer base, suggesting that they were not locally wind-driven. They were also largely in geostrophic balance. A complex regression between the array's average velocity shear and horizontal temperature gradient at 100 m (but typical for the rest of the upper thermocline as well) showed a correlation of 0.89 and a spatial phase difference of 89.8°. This suggests that the departures from the one-dimensional heat budget were associated with the

passage of mesoscale fronts or features past the array.

The strongest signals in the vertically resolved temperature-trend term (Fig. 7, top) of the upper-ocean heat budget (1) were below the mixed layer, in the upper thermocline. The temperature trend, and all the rest of the records that will be displayed in the upper-ocean heat budget, have been low-pass-filtered (after all calculations) with a 96-h cutoff to eliminate variations associated with the dominant tidal (M_2, 12.4 h), diurnal (24 h), and inertial (44.9 h) periods. The strong signals in the temperature trend, localized to the upper thermocline, occurred in November and December, near the beginning of the NE Monsoon, and again in late July, after the peak of the SW Monsoon, concurrent with the strongest velocities and largest
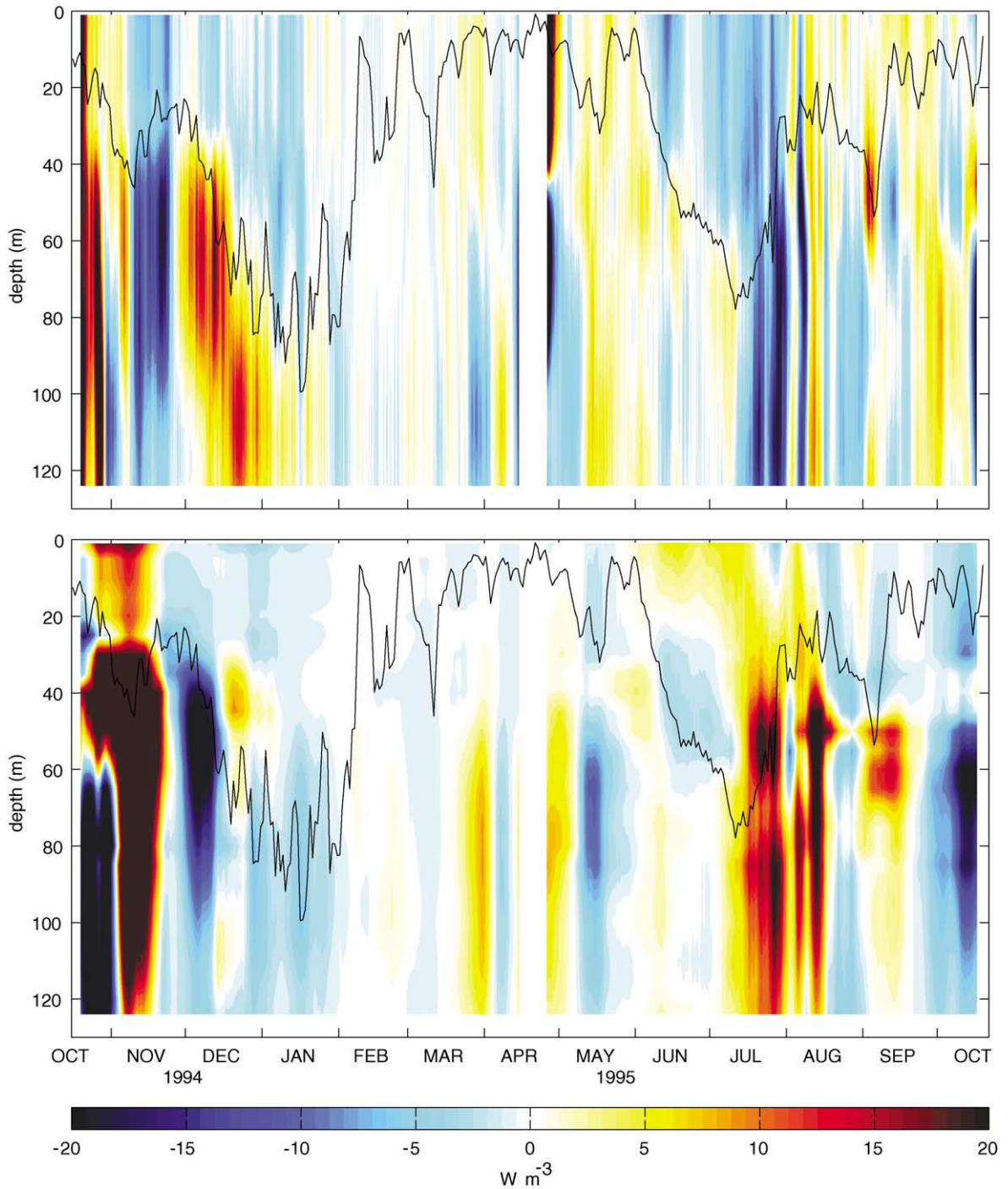
Fig. 7. The vertically resolved temperature trend (*top*) and horizontal heat advection (*bottom*), both 96-h lowpass filtered, with the daily mean mixed-layer depth (*black line*). The horizontal heat advection has a large error associated with it (see following figure), though the large signals below the mixed layer in October–December and July–August are above the error level.

excursions in thermocline depth. There was also a signal of mixed-layer cooling throughout the mixed-layer deepening periods of the NE and SW Monsoons.

These strong signals in the temperature trend were in many cases roughly matched by oppositely-signed signals in the vertically resolved horizontal heat flux (Fig. 7, bottom). These signals were also strongest within the upper thermocline, below the mixed layer. In fact, during the first deployment almost none of the signal within the mixed layer was significantly above the uncertainty (see Fig. 8), while in the second deployment the mixed layer's horizontal heat flux was marginally significant, and positive (cooling). The horizontal heat flux is dependent on the product of velocity and the gradient in temperature, and its uncertainty is thus dependent in part on the magnitude of the velocity, making it a function of time. Below the mixed layer, the signal was strongest again in the early NE and late SW Monsoon, linked with thermocline variability and strong currents. This contrast across the mixed-layer base during the NE Monsoon suggests the advection of variability past the moored array in the upper thermocline, topped by a fairly uniform mixed layer. The mixed layer was not as horizontally homogeneous during the SW Monsoon.

The vertically integrated heat budget (Fig. 9) confirms the suggestion that the temperature trend and horizontal advection of heat, integrated between the surface and 125 m, have a rough balance when the signals are large. This rough balance existed from the beginning of the deployment through the early NE Monsoon (October–December 1994), during a short period in May, and in the late SW Monsoon (July and August 1995). The surface heat flux, by comparison, was unimportant in the heat budget integrated from the surface to 125 m. It is important to note that this vertically integrated heat budget must be differentiated from a mixed-layer heat budget, since in some ways the calculation here underestimates the importance of the surface heat flux. The entrainment flux at the mixed-layer base, an important term in the evolution of the SST, is driven by both the surface heat and momentum fluxes. This turbulent entrainment flux was not measured, and attempts at estimating it through parameterization were overwhelmed by the estimated uncertainty, necessitating the integration to a fixed depth below the influence of surface-driven turbulent fluxes. So while the surface heat flux was dwarfed by the estimated size of the temperature trend and horizontal advective flux (Fig. 9), the horizontal heat flux integrated over just the mixed layer was only significantly different from zero for a few weeks during the SW Monsoon. While allowing for the error in the estimate of the horizontal heat flux, this nevertheless implies that surface-driven processes are important in changing SSTs during the rest of the
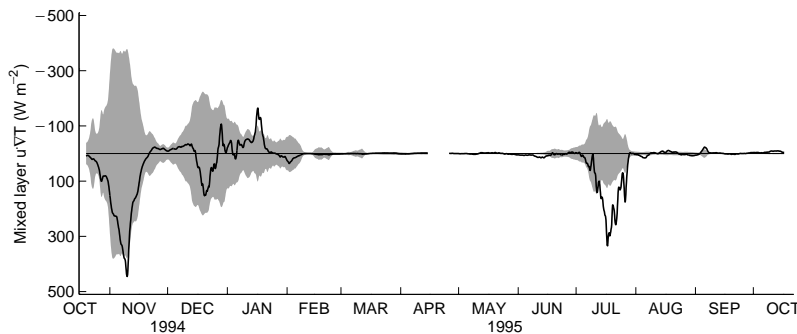

Fig. 8. The horizontal advection of heat integrated only over the daily average mixed-layer depth (as measured at the central WHOI mooring), with the time-varying uncertainty shaded grey. The only significant (above error level) strong horizontal advection within the mixed layer occurs during the SW Monsoon in July, a cooling. There are only two very short periods during the NE Monsoon when the horizontal heat flux is above the level of error in the calculation. Note the y-axis direction is positive downwards.
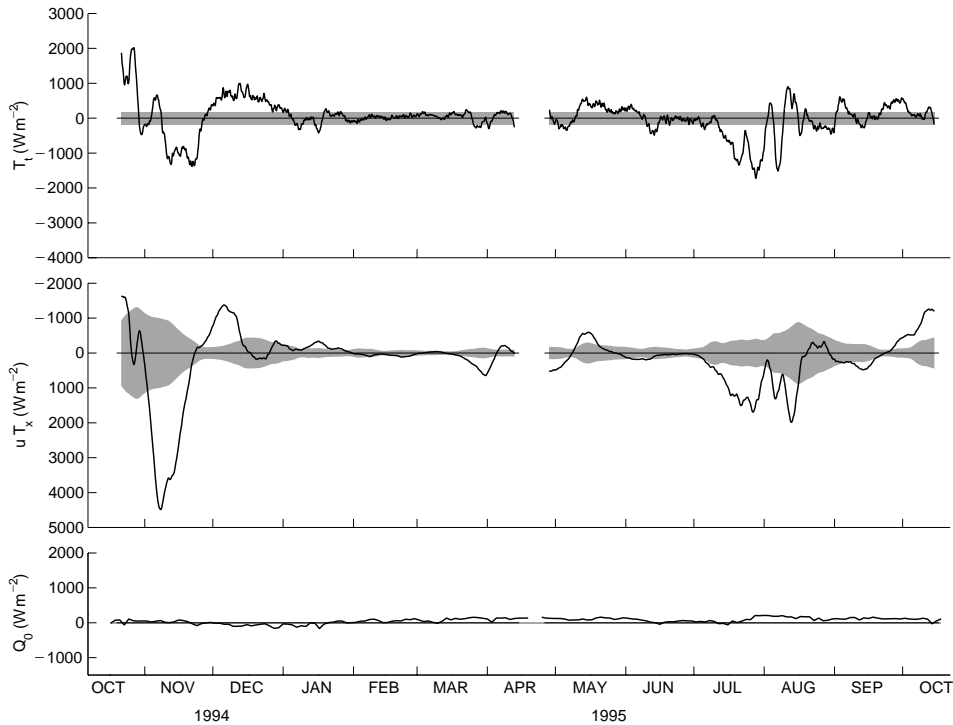
Fig. 9. Terms in the heat budget, vertically integrated between the surface and 125m: the time trend (*top*), horizontal advection (*middle*), and the surface heat flux (*bottom*). Uncertainty is marked by the grey shading about zero. The *y*-axis scale for horizontal advection is reversed, the temperature trend and horizontal advection terms tend to roughly cancel each other.

year. During the net surface heating in the early SW Monsoon, for example, the only process acting to cool the SST is wind-driven entrainment. At other times during the year, horizontal fluxes deeper in the water column vary what the mixed layer entrains into, and SSTs are forced by a combination of surface and horizontal heat fluxes.

The residual term in the heat budget, representing the vertical heat flux due to Ekman pumping or other vertical motions (as well as potentially unresolved processes), yields an estimate of the vertical velocity necessary to close the heat budget. The vertical velocity is assumed to linearly decay to zero at the surface, and w is calculated at 125 m, at the base of the vertical integration (as in Price et al., 1978). The result (Fig. 10) shows that several strong episodic downwelling events, and some smaller upwelling events are necessary to close the heat budget. The strength of these vertical velocities, up to $0.02\,\mathrm{cm\,s^{-1}}$, corresponds to

velocities up to $18\,\mathrm{m\,day^{-1}}$. This is consistent with the velocities reported in the vicinity of strong fronts, estimated from closing heat and mass budgets (Rudnick and Weller, 1993), as well as those reported in the vicinity of a coastal upwelling filament in the California Current system, estimated from a density and velocity survey (Shearman et al., 1999). In this case they are more often downwelling, since the estimate of the horizontal heat flux is generally more cooling (positive) than the temperature trend.

A number of studies (e.g., Bauer et al., 1991; McCreary et al., 1993) have emphasized the role of Ekman pumping in setting the mixed layer's depth structure across the Arabian Sea. Both noted the generally deeper mixed layers to the south and east of the Findlater Jet wind axis and shallower mixed layers towards the Arabian coast, consistent with open-ocean Ekman upwelling and downwelling. Lee et al. (2000) revisited this idea by examining
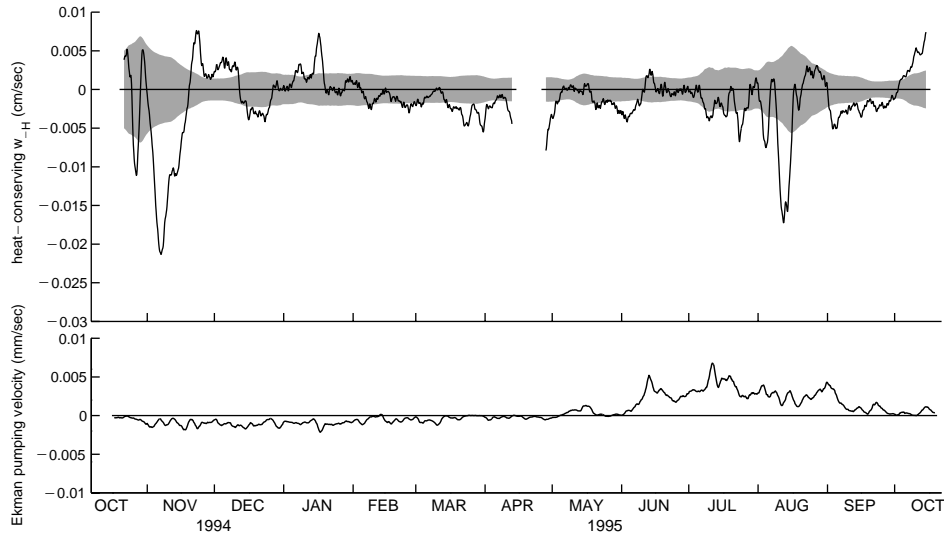
Fig. 10. (a) The derived vertical velocity from closing the heat budget. Uncertainty marked by the grey outline about zero. (b) Ekman pumping at the site of the mooring as estimated from ECMWF wind stresses. This estimate of vertical velocity is much smaller (scale is an order of magnitude larger than (a) to render the variability visible) than that derived from closure of the heat budget.

climatology, and found that local surface forcing (entrainment driven by wind and/or heat forcing) had a much stronger effect than Ekman pumping on the mixed-layer depth, though neither, nor their combination, could fully explain the observed patterns of mixed-layer depth. An estimate of the Ekman pumping at the moored array, calculated from wind stresses from the European Centre for medium-range weather forecasts (ECMWF), is shown in Fig. 10b. The magnitude of the vertical velocity is quite small ($<1 \, \text{m day}^{-1}$), certainly much smaller than the estimates of what is required to close the heat budget. It also has the wrong sign, so at the site of the moored array, Ekman pumping appears to make a very small contribution to the heat budget and mixed-layer deepening.

How representative is this moored time-series for the interior of the Arabian Sea? The decorrelation time-scales of temperature measured at the moored array are on the order of 30–40 days, so the record has sampled about ten of these time-scales. In reality, only two major events passed by the array in the year it was deployed, so the mean heat budget captured here cannot be considered representative of the long-term mean. However,

the fact that horizontal advection is important in the Arabian Sea is upper-ocean heat budget remains a robust conclusion.

3.2. Remote sensing insights

The moored record showed two major episodes of strong horizontal advection (Fig. 4), during the beginning of the 1994 NE Monsoon, and during the latter part of the 1995 SW Monsoon. The discussion here is likewise split.

3.2.1. Northeast monsoon

The moored array was set in October 1994 during a period of strong horizontal advection, which alternated in sign through December 1994 (see Fig. 9) from initially negative (warming) to positive (cooling), then back to negative. The dynamic height and altimetry (Fig. 2) correspondingly show relatively low sea-surface height (SSH) at the time of deployment, immediately growing to high SSH through the end of October, decreasing during November, then increasing again through December. These were accompanied by strong surface currents changing direction from east and southeastward during October and November to
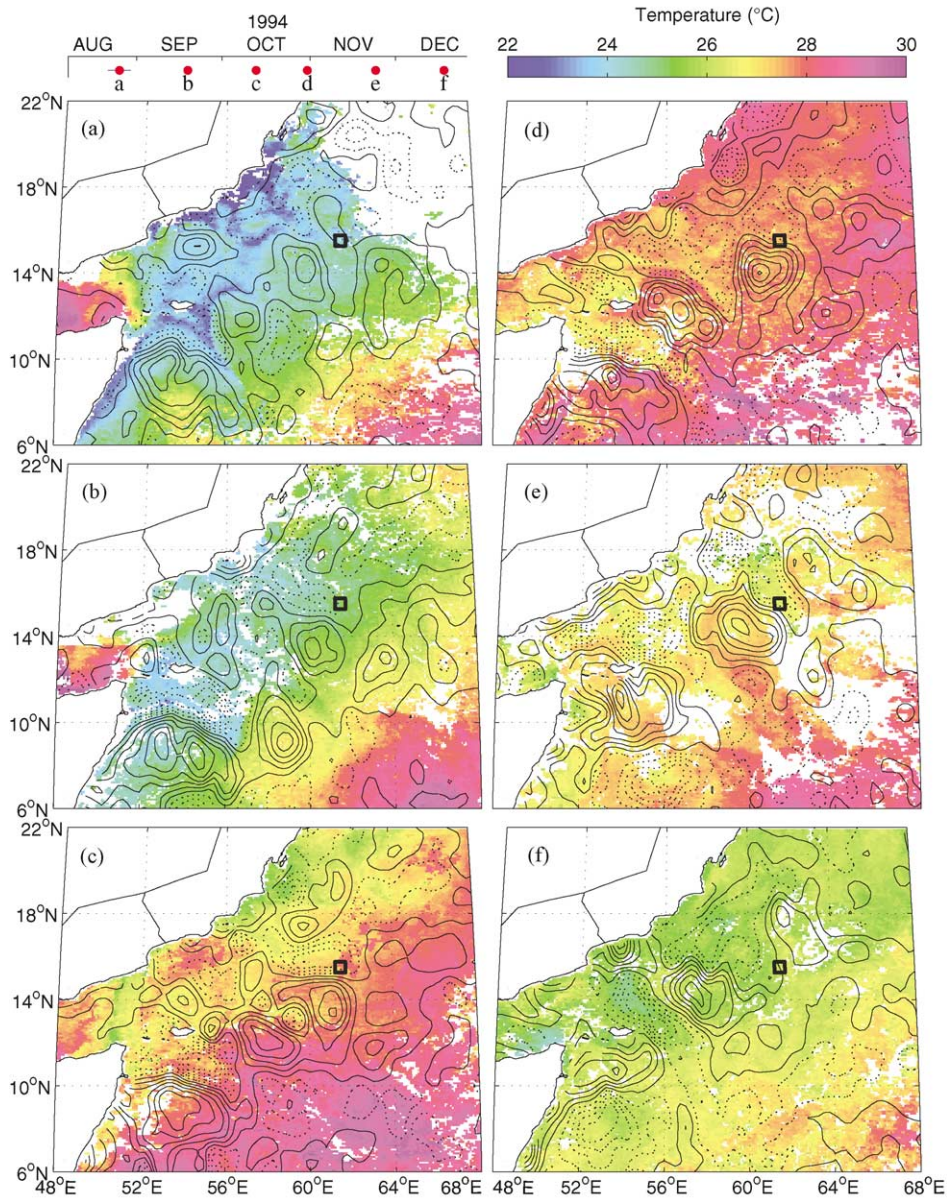
Fig. 11. NE Monsoon time-series maps of altimetry and SST. Contours of SSH (every 5 cm, solid for positive, dashed for negative) overlaid on the concurrent AVHRR SST imagery, where white indicates cloudiness. The panels $a - f$ are in chronological order, marked by the axis in the extreme upper left.

north northwestward during December (Fig. 3). The temporal evolution of the surface fields in SSH and SST for this period are illustrated in Fig. 11c–f, covering 13 October–18 December 1994.

The interactions and movement of a pair of eddies are responsible for the strong observed horizontal fluxes. Following the sequence from Fig. 11c–f, the moored array starts in the interior of a cyclonic eddy (c), then encounters the edge of

a strong anti-cyclonic eddy (d). As this eddy pair propagates westward, the moored array again samples the cyclonic eddy (e), then encounters a weaker anti-cyclonic eddy east of the original pair (f). In conditions of baroclinic, surface-intensified currents in geostrophic balance, all demonstrated true in the previous section, locally high (low) SSH will correspond to a deeper (shallower) thermocline. In a comparison of current-meter moorings and altimetry, Wunsch (1997) came to the qualitative conclusion that the altimeter tends to reflect the movement of the thermocline, described by the first baroclinic mode. The overview of the array temperature (Fig. 5) then matches the interpretation from the altimetry, with variations in the thermocline depth matching the passage of the eddies. The sequence of currents is also consistent with the altimetry, with the strong east and southeastward currents in October and November (c, d, e) followed by a north northwestward current in December (f).

While the changes in the SSH at the moored array were large, the gradients in temperature revealed by the SST images were far less dramatic, not exceeding about 0.7°C across the eddy pair (Fig. 11e). Towards the end of the NE Monsoon (f) they were even smaller, and the SST across a large region of the basin was quite uniform, in contrast to the stronger gradients seen at the onset of the NE Monsoon (c). SST was also everywhere reduced following the only extended yearly period of surface cooling over the basin. This is consistent with the vertically resolved heat flux at the moored array (Fig. 7) and the mixed-layer horizontal heat flux (Fig. 8), both of which show weak heat fluxes within the mixed layer, not significantly different from zero.

The eddy pair continue to evolve away from the moored array, finally dissipating near the Arabian coast well after the NE Monsoon. Their propagation speed was about $10 \, \text{cm} \, \text{s}^{-1}$, just slightly higher than the estimated phase speed of $9.0 \, \text{cm} \, \text{s}^{-1}$ for the first baroclinic mode linear Rossby wave, as expected for the tropics (Chelton and Schlax, 1996). The Rossby wave speed was estimated from the vertical structure eigenfunctions of a buoyancy frequency profile measured by CTD at the moored

array during the initial deployment, assuming long waves.

The origin of these mesoscale eddies can be traced back in time several months before the mooring deployment. They first appeared as meanders of the Somali Current extension, which was a variation of the Socotra Eddy (Fischer et al., 1996) in the 1994 SW Monsoon, separating warmer interior waters from cooler upwelled water to the north and west (Fig. 11a). The development of these eddies from the Somali Current extension may explain the sharpness of the front separating the anticyclonic and cyclonic eddies in the sampled pair. The 1994 SW Monsoon seems to have a particularly well-defined Somali Current extension compared to the 1995 SW Monsoon. Towards the end of the 1994 SW Monsoon, the Somali Current extension was clearly defined in the SST by a sharp gradient of over 2°C, and its meanders were captured in the altimetry. It extended more than 600 km northeast of Socotra, nearly to the site of the array. By contrast, during the 1995 SW Monsoon, the Somali Current extension seemed far less organized, and more limited to the vicinity of Socotra Island (and more typical of the Socotra Gyre described by Fischer et al., 1996). The range and breakup of the Somali Current extension then appears to have implications for modulation of the upper-ocean heat budget long after each SW Monsoon season.

3.2.2. Southwest Monsoon

The temporal variability in the 1995 SW Monsoon (June–September) heat budget for the moored array showed the first major episode of cooling horizontal advection both within the mixed layer and below during the latter part of the SW Monsoon (late July–early August). This period from late July through early August was marked by a sharp and sudden decrease in the SSH (Fig. 2) and accompanied by strong eastward than southeastward currents (Fig. 3). The temperature and salinity profiles (Fig. 5 and Fig. 14) showed large changes during this time period. The temporal evolution of the SSH and SST fields during this period is illustrated in Fig. 12.

The development of a broad swath of coastally upwelled water was evident in the June SST
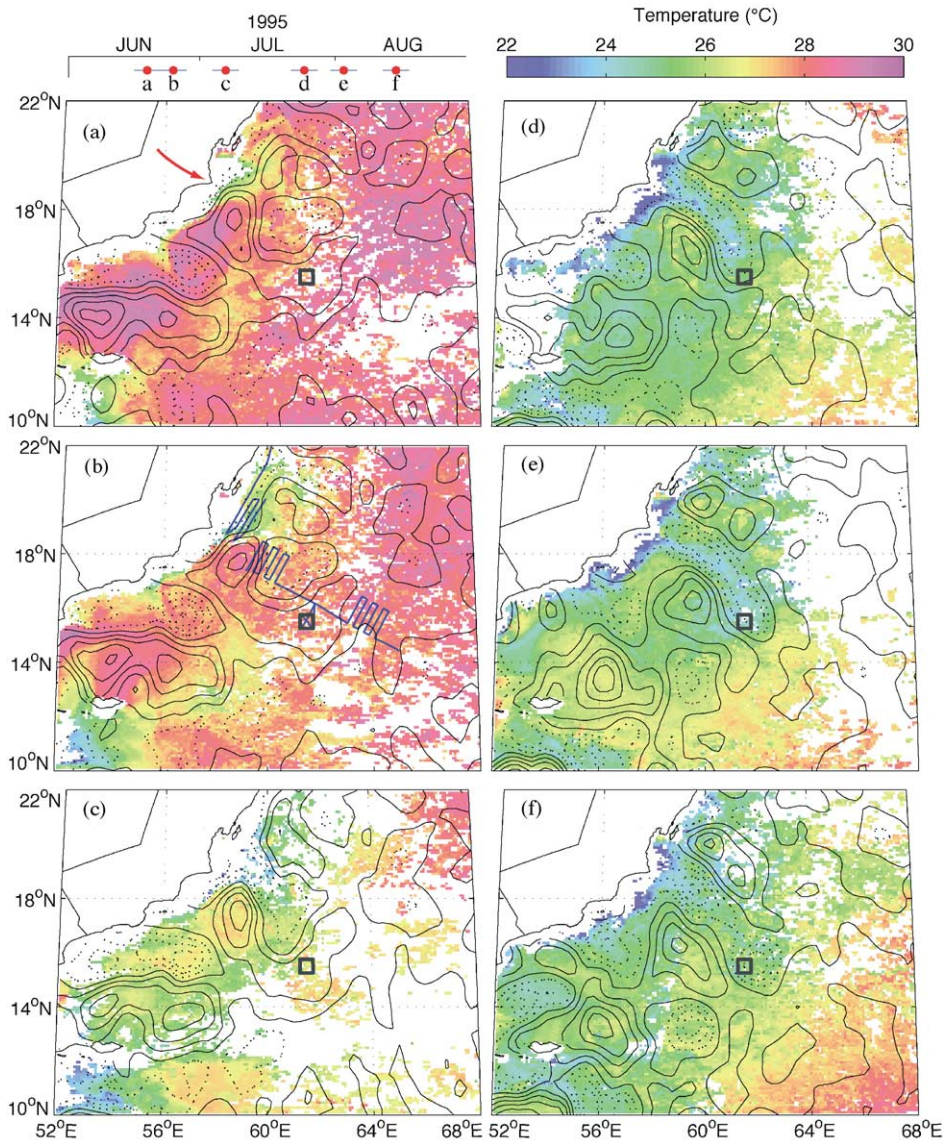
Fig. 12. SW Monsoon time-series maps of altimetry SSH and SST imagery. Contours of SSH (every 5 cm, solid are positive, dashed negative) are overlaid on the AVHRR SST imagery. The panels *a–f* are in chronological order, with the times given by the axis in the extreme upper left. The red arrow in *a* points to Ras Madrakah, while the blue lines in *b* represent the SeaSoar survey track during this period.

imagery (Fig. 12a and b). By June 1995 the ECMWF wind analysis had a broad scale pattern of southwesterly winds, driving coastal upwelling along the Omani coast. Clouds tended to form as the moist, nearly saturated air of the SW Monsoon (Weller et al., 1998) met cool, upwelled water,

often obscuring the view of the SST in these regions. This was apparent along the coast in the entire 2-month sequence depicted in Fig. 12.

As early as mid-June there was evidence of the offshore transport and development of a filament of cold, upwelled water off of Ras Madrakah

(arrow in Fig. 12a). The filament continued to develop through July, finally reaching the moored array in late July (Fig. 12b–d). In its early stages, the filament appeared to be influenced in part by an anti-cyclonic eddy to its south. A detailed SeaSoar survey of the filament was made from 20 June to 3 July 1995, the track of the survey is shown in the concurrent panel of SSH and SST (Fig. 12b).

The development of the filament included strong offshore transport of cool water that reached the moored array in late July (Fig. 12d). This was concurrent with the sharp drop in the observed dynamic height and SSH observed at the moored array (Fig. 2). The temperature at the array also showed a sudden shoaling of the thermocline and cooler surface water (Fig. 5), coincident with strong heating (see Fig. 4). The SST imagery showed a difference between the filament and surrounding waters of about 2–3°C, consistent with the observed drop at the moored array, and much stronger than the gradients observed during the NE Monsoon.

The evolution of the filament after its initial influence on the moored array was slow, and it appeared to fall apart while its surface signal subsided. The weakening of the strong, offshore, jet-like transport was evident through early and mid-August (Fig. 12e and f). The SST signature of the filament was obscured by clouds, but the altimetry showed a further separation of the weak cyclonic feature at the end of the filament (Fig. 12f) with a disappearance of any noticeable remnants by the end of September 1995.

Moving in the other direction in time, the anticyclonic feature that formed the southwestern boundary of the filament first appeared in the altimetric record in mid-May of 1995, several hundred kilometers offshore and east of Ras Madrakah. This supports the contention of Manghnani et al. (1998) that coastal filament formation is dependent on the details of the mesoscale-eddy field. A similar linkage between the mesoscale-eddy field and the complex flow and filaments of the California Current system has been made (Brink and Cowles, 1991; Strub et al., 1991; Shearman et al., 1999).

3.2.3. Discussion

While the propagation of the NE Monsoon eddy pair away from the moored array seems to follow linear Rossby wave dynamics with a nearly matching phase speed, the time-longitude slice at 15.5°N, the central latitude of the array (Fig. 13), indicates that this particular eddy pair is the strongest wave-like signal. The SSH anomalies are generally larger to the west of the array longitude, and smaller to the east, and there is evidence of westward propagation of features, particularly to the west of the array. The filament is observed as a strong depression of the sea surface in August, and there is no clear signal of its propagation westward.

Eddies play a clear role in modulating the heat flux at the site of the mooring, and mesoscale eddies are widespread in the Arabian Sea. During the US JGOFS Process Study, Flagg and Kim (1998) found, using shipboard ADCP data, that upper-ocean currents in the northern Arabian Sea were dominated by mesoscale eddies throughout the year, with eddy kinetic energies that were eight times larger than the mean kinetic energy, and larger near the coast. Kim et al. (2001), using concurrent TOPEX altimetric data, added to this result, finding the highest levels of sea level variability within 400 km of the Omani coast, with elevated levels of variability during the SW Monsoon. Using 7 yr of the combined TOPEX/ERS altimeter data over the Arabian Sea, we found (for details see Fischer, 2000) elevated levels of eddy kinetic energy (EKE) during the SW Monsoon in a region extending offshore about 400 km southeast from Masirah Island and another between Socotra and the Arabian coast south of Ras Mirbat, in agreement with the results of Kim et al. (2001). In addition, we found a statistically significant region of elevated EKE in a broad region of the Arabian Sea centered about 64°E, 12°N, southeast of the moored array. One possibility explaining this region is that instabilities of the accelerating directly wind-driven currents created by the onset of the monsoon could develop into mesoscale features.

The elevated levels of EKE along the Arabian and Somali coasts during the SW Monsoon are particularly relevant, since these eddies may
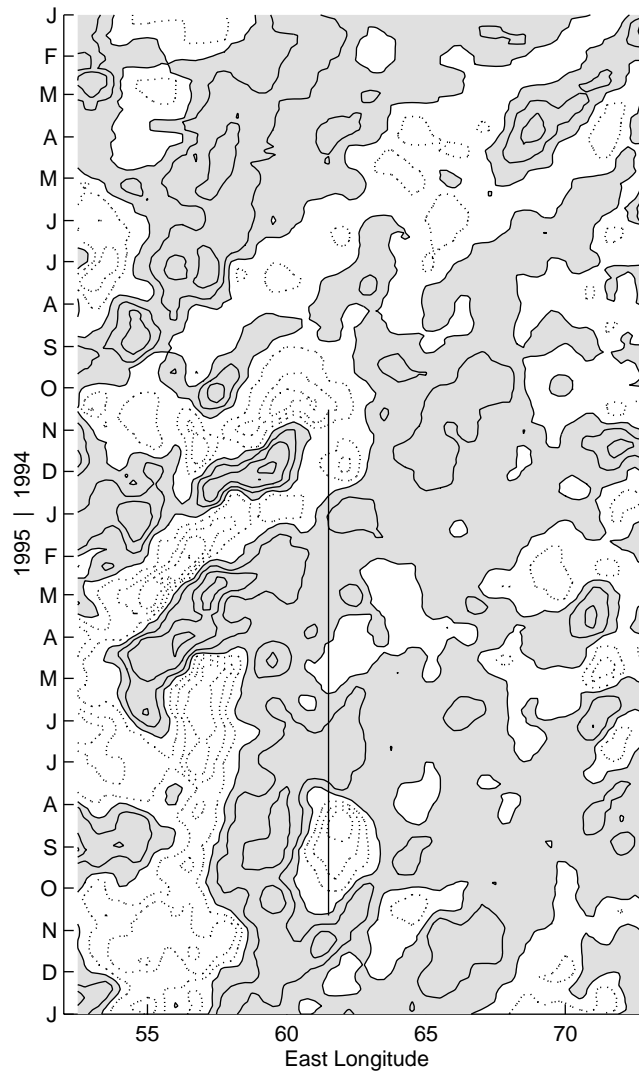
Fig. 13. Time-longitude plot of SSH anomaly at the latitude (15.5°N) of the mooring, with the longitude and duration of the mooring deployment marked by the vertical line. Contours (positive solid with grey shading) every 5 cm. There is evidence of westward propagation of anomalies. The coastal filament appears as a localized area of low SSH during July–September of 1995 at the longitude of the mooring.

transport coastally upwelled water offshore, a process captured by the moored array. This offshore transport of coastally upwelled water then plays an important role not only in the upper-ocean heat budget, but also directly in the SST evolution.

3.3. Water mass properties and the mesoscale flow

Further in situ observations taken concurrently with the moored array observations allowed a

clearer view of the events of the SW Monsoon, and demonstrated that coastally upwelled water did advect out to the site of the mooring, transported by a filamentary mesoscale feature.

3.3.1. Water mass changes during advective events

At the time of the SW Monsoon SeaSoar survey, coastally upwelled water was just beginning to be advected offshore (Fig. 12b). The inner, filament radiator was nearly entirely within the upwelled

water. Two sections from the filament radiator are shown in the upper panel of Fig. 14. Section A ranges from 50–100 km offshore, while Section B is about 75 km farther offshore. The southwestern corner of Section B has some of the high surface salinity (36.3 and greater) water characteristic of the Arabian Sea as a whole. The strongest filament velocities were associated with the strongly tilting isotherms in this southwestern corner. The surface waters on the coastal side of this front had characteristics (salinity <36.2 and temperatures <25°C) of deeper water (100–150 m) farther offshore, with slightly elevated temperatures consistent with solar heating. Both sections (and the entire filament radiator) were primarily composed of this fairly low-salinity and low-temperature water. There was a fair amount of interleaved structure in the salinity data, including large masses of water concentrated below 200 m with the characteristic high salinity of Persian Gulf water, which mixes in along the 26.6 isopycnal surface from high salinities (up to 37 in the Gulf of Oman, here diluted by entrainment to 36.2, Wyrtki, 1971).

Coincident in time with the strongest horizontal heat fluxes of the SW Monsoon (Fig. 9 late July–early August), the salinity and temperature structure at the moored array changed suddenly (Fig. 14, bottom panel). The high surface salinity that had been characteristic of the record was replaced with surface salinities that were the same as those found in the upper thermocline. Temperature dropped throughout the water column. At the same time the net surface heat flux (Fig. 4) increased dramatically, denoting a coupling between the oceanic surface temperature and the surface heat flux.

A comparison of the temperature-salinity (TS) properties of the coastally upwelled water sampled by the SeaSoar survey and the changing TS properties observed at the mooring confirmed that coastally upwelled water did in fact move to the site of the moored array. The SeaSoar filament radiator was surveyed from 21–24 June 1995, nearly 1 month before the observed change in TS properties at the moored array. The entire filament radiator is tagged as 'filament' water whose TS properties are shown by the black points in the left panel of Fig. 15. The grey points are from the sampling by the SeaSoar in the butterfly pattern made around the moored array (29–30 June 1995), and are representative of the composition of offshore waters. The right-hand panel in Fig. 15 shows TS properties measured at the UW-S mooring during two different time periods, separated by the strong advective event, which are marked by the black and red bars on the time axis at the bottom of the lower panel of Fig. 14. The grey points are for the period from 12 to 18 July 1995 before significant advection had taken place, representative of the water mass properties at the moored array in the early part of the SW Monsoon. The black points are for the period from 1 to 11 August, after a period of strong horizontal advection.

The grey points in each panel map out similar water masses, with high salinities in the near-surface compensated by much warmer temperatures, and are typical profiles for the interior of the Arabian Sea during the SW Monsoon. The black points in each panel are from observations separated by about 500 km and 1 month in time, so similarities between the two, and differences from the mean SW Monsoon TS properties (grey), are strong indicators of offshore transport of coastally upwelled water, as suggested by the SSH and SST imagery. In the SeaSoar survey, there were two primary differences between the onshore (black) and offshore (grey) properties. In the deepest portions of the survey there was a strong presence of saline (35.9–36.2) water on the 26.0–26.5 isopycnals, compensated in temperature. This was the upper, diluted part of Persian Gulf water (Wyrtki, 1971) which makes its way from the Gulf of Oman along the Omani coast, often in discrete masses. The other major difference came

Fig. 14. Sections across the SW Monsoon filament, through space using the SeaSoar (*top*, with inset map showing the location of the two sections, both from the 'filament radiator' closest to the coast), and in time at the UW-S mooring (*bottom*, where bars indicate times extracted in Fig. 15).
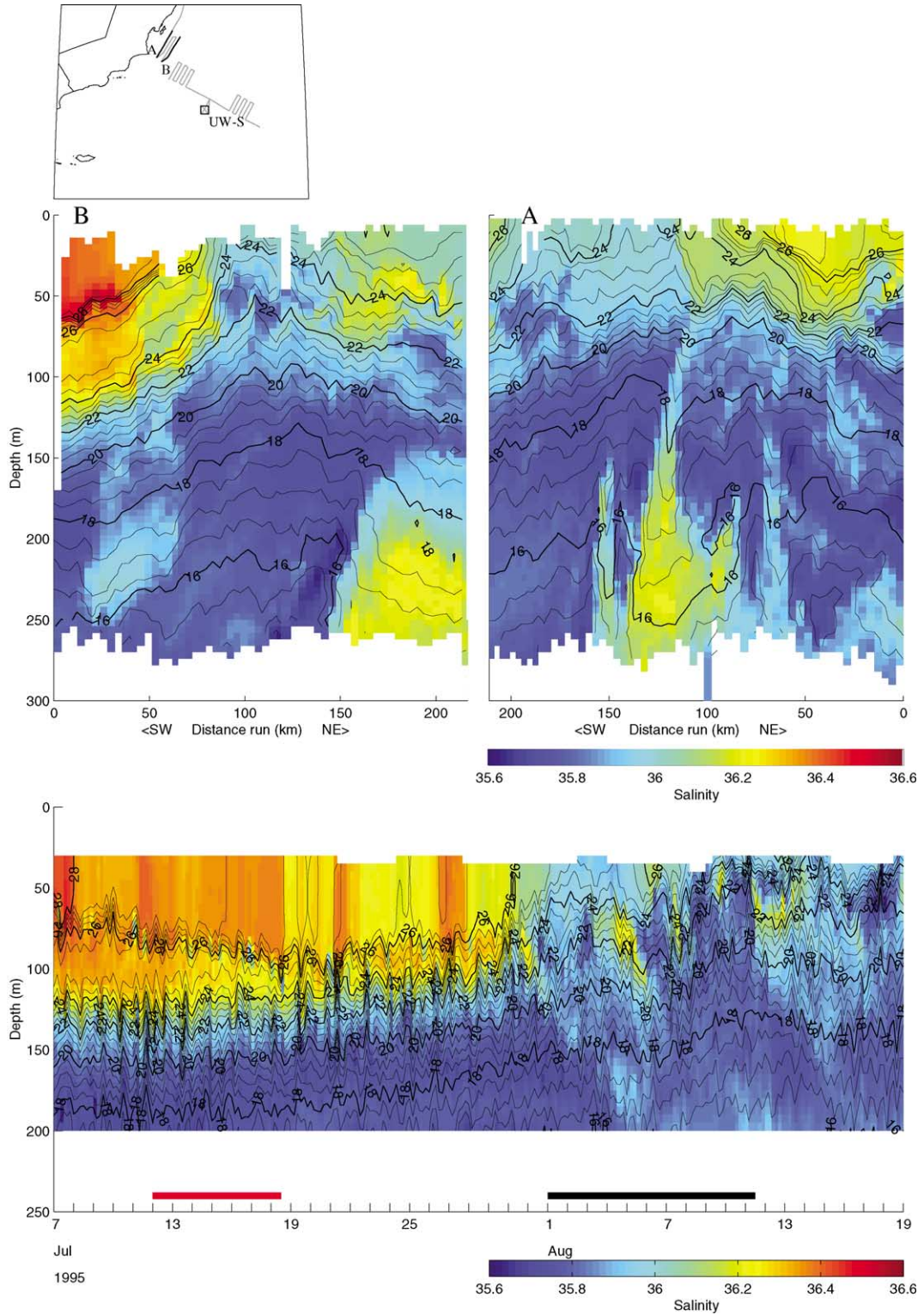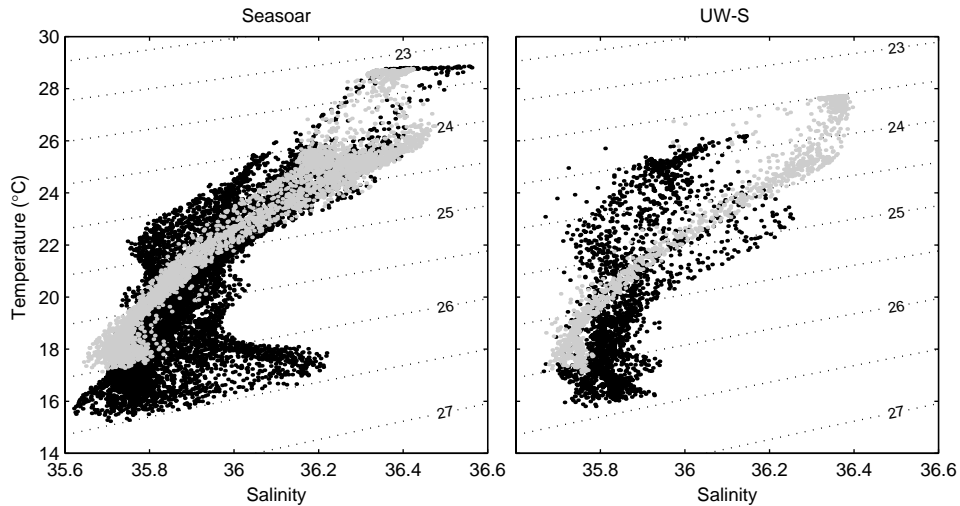
Fig. 15. TS diagrams depicting the difference between the mean offshore water mass during the SW Monsoon (*grey*) and the coastally upwelled water (*black*). The left panel shows SeaSoar spatial data, while the right panel shows the UW-S moored time-series data. The distinguishing characteristics of the upwelled water are the two lobes above and below the curve defining the mean SW Monsoon offshore water mass. The lobe above is coastally upwelled water that has been in contact with the atmosphere, warming it, while the lobe below contains remnants of the Persian Gulf outflow.

in lighter density classes, where waters with salinities between 35.8 and 36.2 appeared closer to the surface and warmer than in the offshore survey. A reasonable inference is that deeper waters are drawn to the surface in coastal upwelling, then undergo transformation (heating) under the influence of air–sea fluxes. The surface heat fluxes estimated from bulk measurements made aboard the R/V *Thompson* were strongly positive in the filament survey (about 200 W m^{-2} in the daily average), and remained positive in the inshore radiator survey (about 100, W m^{-2} Lee et al., 2000).

The strong horizontal advection at the site of the moored array 1 month later brought with it water with quite different TS properties. Like the coastally upwelled water sampled by the SeaSoar, at the deepest range (around 200 m) there was an increase in density (up to 26.5) and an increase in salinity. Though it was not as pronounced as the strong salinities on the 26.5 isopycnal sampled by the filament survey, this is indicative of some mixing with Persian Gulf water. Near the surface, salinities were lower than before, more typical of mid-depth

(100–150 m) waters previously, but had higher temperatures than those observed in the filament survey. This is again consistent with contact with the atmosphere under the strong surface heating of the SW Monsoon. Taken together, the filament SeaSoar survey and the changing TS properties at the fixed point of the moored array suggest that coastally upwelled waters made their way from nearshore areas to at least 600 km offshore at the site of the moored array.

In contrast to the lasting change in water mass properties brought by the coastal filament, the changes during the strong horizontal heat advection of the NE Monsoon were smaller and more temporary. The evolution of TS properties observed at the UW-S mooring under the influence of the sequence of cyclonic and anticyclonic mesoscale features passing by the moored array was confined to intermediate depths. Water in this depth range (between the 24 and 26 isopycnal surfaces, all above 200 m) became fresher under the influence of the first anticyclonic mesoscale feature (Fig. 11d), then saltier with the cyclonic feature (Fig. 11e), and fresher again with the

passage of the next anticyclonic feature (Fig. 11f). The front associated with the formation of these eddies during the 1994 SW Monsoon acted as a boundary between two water masses below the mixed layer, and moved back and forth across the moored array through the NE Monsoon.

3.3.2. Structure and transport of the SW Monsoon coastal filament

The surface temperature forcing was stronger and more variable than the surface salinity (evaporation–precipitation) forcing in the Arabian Sea (Weller et al., 2002), and the halocline quite sharp, making salinity a better tracer of water masses than temperature in the upper ocean. At the site of the mooring and in the offshore regions of the SeaSoar survey during the SW Monsoon, the 36.1 isohaline surface fell between 100 and 150 m in depth, in the upper thermocline. Very close to the coast it outcropped, and was a good marker of the strong front between the coastally upwelled and offshore waters. The shape of this surface in the SeaSoar survey is indicated in Fig. 16a. The surface outcropped along the southwestern and northeastern edges of the filament radiator, then outlined the extension of the filament through the center of the inshore radiator. It did not outcrop in this region, but appeared very close to the surface in the northeastern portion of the inshore radiator, descending to about 50–60 m as the filament extended offshore. The surrounding waters, at the southwestern end of the filament radiator and surrounding the filament in the inshore radiator, were much like the waters observed offshore, with the 36.1 isohaline surface between 100 and 150 m in depth, though seemingly deeper on the southern and western sides of the filament.

The temperature along the isohaline surface increased markedly as it outcropped, from about 22.5°C to about 25.5°C, still well below the surface temperatures farther offshore. At the time of the survey, the SW Monsoon winds had been active for nearly a month, inducing coastal upwelling for as long. One month of a 200 W m^{-2} surface heat flux will heat a layer 50 m deep by 2.5°C. The mixed layers in the filament survey were <30 m deep, in some cases shallower than 10 m, the nominal minimum depth of the SeaSoar survey. As the filament moved offshore, the 36.1 isohaline surface deepened, and the temperature on the surface increased, up to a maximum of 26.5°C. This is consistent with the water mass properties sampled earlier in the filament life (from SeaSoar) and later at the moored array. The filament also outlined a region of shallower mixed-layer depth and cooler mixed-layer temperature (Fig. 16b), again consistent with the sudden shoaling and cooling of the mixed layer observed at the moored array when the filament arrived in late July.

The coastally upwelled water and the filament were also associated with increased productivity (Brink et al., 1998), seen in the chlorophyll *a* concentrations observed in the survey (Fig. 17), perhaps provoked by the strong local vertical velocities associated with the mesoscale, inferred as the filament passed the moored array, or associated with the coastal upwelling itself. The highest concentrations occurred in the top 50 m, and remain elevated along the filament, though there was a decrease from the concentrations found closest to the shore. There was also considerable patchiness along the thin filament in the inshore radiator, highlighting the small scales of chlorophyll *a* noted in Lee et al. (2000). The passage of eddies at the moored array was often coincident with jumps in the observed biological productivity, as seen in elevated chlorophyll *a* levels (Dickey et al., 1998). Moored sensors recorded a peak with the arrival of the coastal filament at the end of July, consistent with the elevated levels found within the filament during the SeaSoar survey. The strongest signal in the moored record, however, is coincident with the horizontal heat flux of an anticyclonic region at the beginning of December. Unfortunately, this was also coincident with the beginning of the negative surface heat flux and the beginning of locally surface-driven convection, so in this case the cause of the bloom, local vertically driven mixing, horizontal advection, or vertical motions associated with the mesoscale eddy, cannot be determined easily. Beyond pulses in near-surface productivity, pulses in the mass flux, organic and inorganic carbon flux, and biogenic silicate and calcium carbonate fluxes out of the euphotic zone
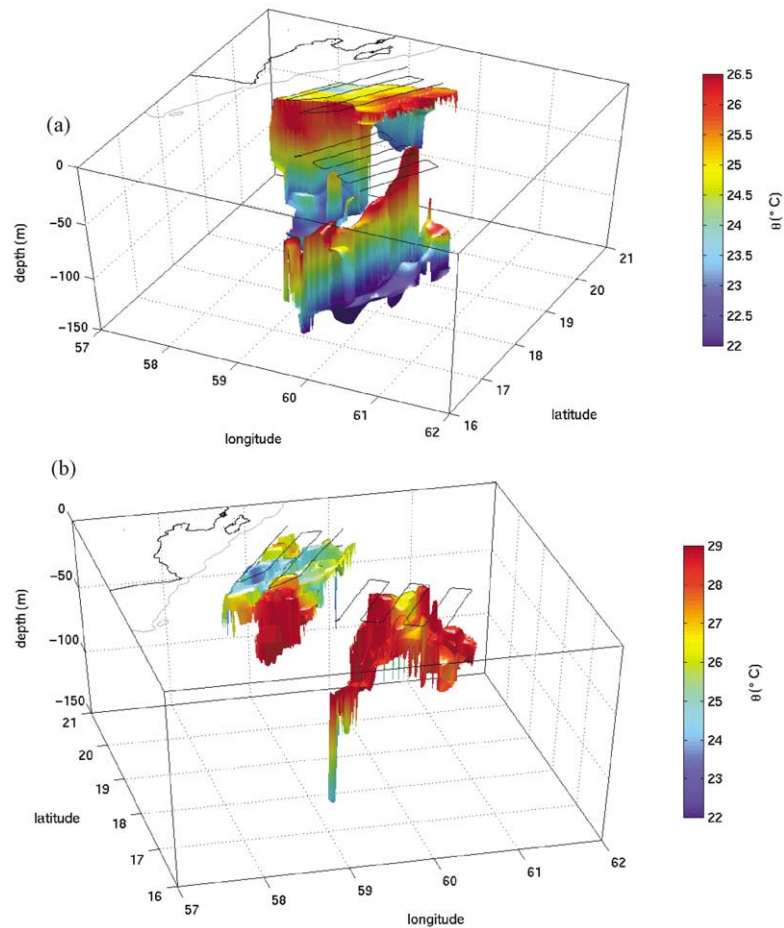
Fig. 16. (a) A visualization of the temperature (θ) on the surface of constant 36.1 salinity, from objectively mapped SeaSoar data. In the filament radiator (track closest to shore, the inshore radiator is also marked), the 36.1 isohaline surface outcrops, and the temperature shown is the near-surface temperature. (b) Mixed-layer θ on the surface representing the mixed-layer depth. Note that the view angle and color scale are different from (a). The filament has a shallower and cooler mixed layer than surrounding areas. Solid and grey lines are the coast and 200 m isobaths.

were captured in a sediment trap close to the moored array (Honjo et al., 1999), also possibly associated with the passage of the SW Monsoon coastal filament.

Remotely sensed data have already suggested that the filament and its transport not only had a large impact on the local upper-ocean heat budget, but similar variability is likely important in the overall upper-ocean heat budget of the Arabian Sea. Estimates of the volume flux and integrated section heat fluxes through the filament using the SeaSoar survey (Fig. 18) allow us to be more

quantitative. The instantaneous volume flux through each section shown was calculated using the shipboard ADCP data, as an integral of the cross-sectional velocity $\iint \mathbf{u} \cdot \hat{\mathbf{n}} \, ds \, dx$, where $\hat{\mathbf{n}}$ is the cross-sectional normal vector and ds is in the alongsection direction. The integrated section heat flux (as opposed to a true heat transport, which would have a controlled mass) is the integral of the cross-sectional velocity and the difference in the observed potential temperature and a reference potential temperature $\iint \mathbf{u}(\Theta - \Theta_{\mathrm{ref}}) \cdot \hat{\mathbf{n}} \, ds \, dz$. The reference temperature is a guess at what a typical
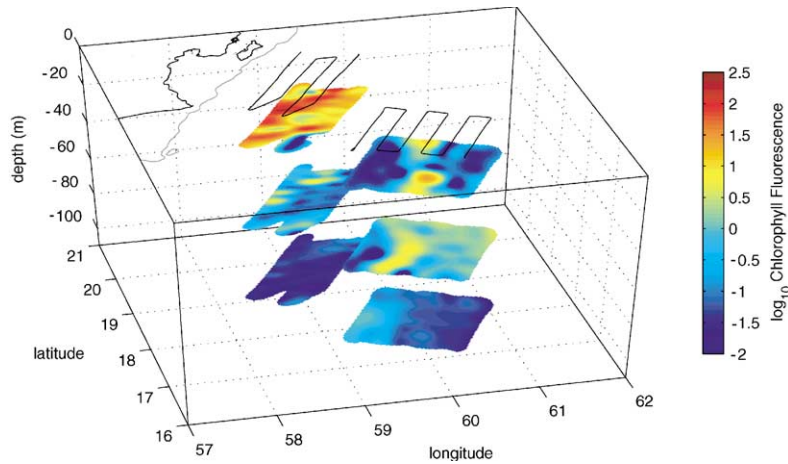
Fig. 17. The chlorophyll *a* concentration at the fixed depths of 16, 62, and 102 m, estimated from chlorophyll *a* fluorescence calibrated with in situ measurements. A strong near-surface maximum is evident in the coastal-upwelling region and in the filament as it extends offshore. Solid and grey lines are the coast and 200 m isobath.
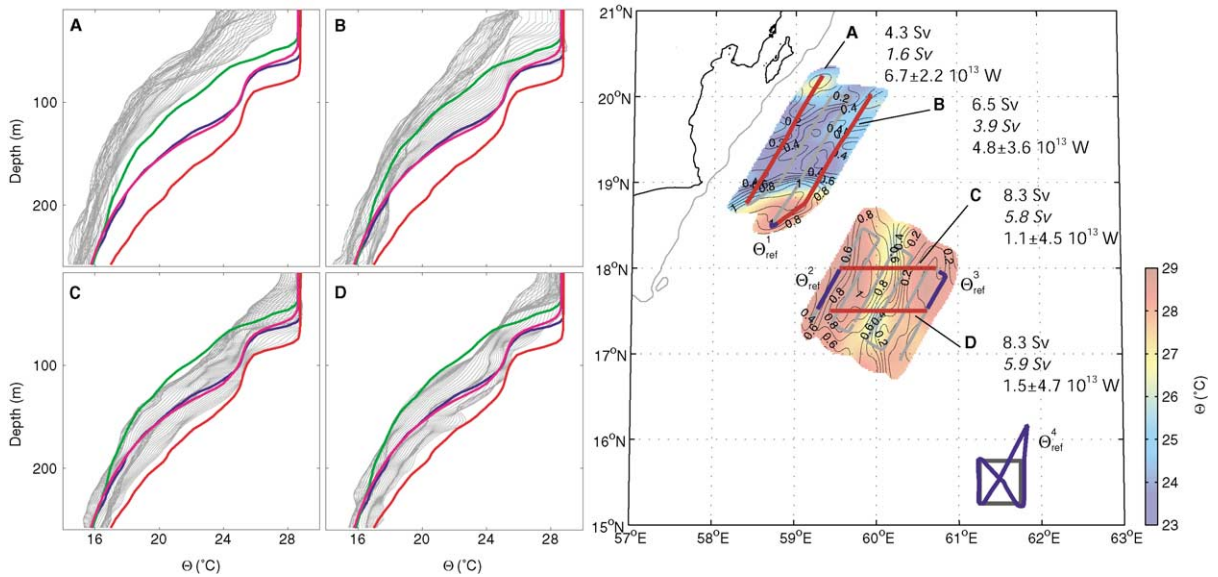

Fig. 18. Estimates of the instantaneous volume flux (first, integrated from 10–260 m in depth; and second, in italics, for water with $\sigma_\theta < 25.0$) and integrated section heat flux of the filament in the SeaSoar survey, across various sections. For orientation, the map on the right shows objectively mapped potential temperature in color, with contours of shipboard ADCP velocity magnitude (in m s^{-1}), at 30 m depth, clearly outlining the filament of cooler water extending eastward offshore, then turning southward. Solid and grey lines mark the coast and the 200 m isobath, and the black square the location of the moored array. Red along the grey SeaSoar track marks the reference sections (A–D), while blue marks regions from which reference temperature profiles were extracted for the section heat flux calculations (marked Θ_{ref} 1–4). The four panels at left are temperature profiles from each section, with grey indicating the section profiles, and color denoting Θ_{ref} (1: blue, 2: red, 3: green, 4: magenta). Estimates of the volume flux and integrated heat flux through each section are noted on the map.

profile for the section was before the intrusion of the filamentary feature, and is a major source of uncertainty in the section heat flux. Four different reference profiles were used, extracted from the SeaSoar data in a number of geographic locations, varying most notably in the depth of the upper thermocline, and the spread provides some estimate of the uncertainty. Uncertainty in the volume flux comes largely from the lack of synopticity in the survey. The vertical integral is limited between 10 and 260 m by the available data. The instantaneous volume flux of water with density $\sigma_\theta < 25.0$, surface waters that likely undergo an irreversible transformation, is also estimated.

The volume flux in the inshore radiator across Sections C and D (which have the same section length) is fairly constant at 8.3 Sv ($1\,\text{Sv} = 10^6\,\text{m s}^{-1}$), 5.8–5.9 Sv for $\sigma_\theta < 25.0$. Sections A and B in the filament radiator have smaller fluxes, though neither section fully crosses the broad maximum in filament velocity, and so should be considered subsamples of the full filament. The section heat flux estimates generally reduce in the offshore direction, but have a large associated uncertainty. The range of values from $1.1–6.7 \times 10^{13}\,\text{W}$ is between 3% and 18% of the total heat change due to upwelling along the Arabian coast, $3.8 \pm 1.9 \times 10^{14}\,\text{W}$, estimated by Düing and Leetmaa (1980) for the SW Monsoon. Assuming a filament lifetime of 2 weeks (suggested by the altimetry and SST imagery), the instantaneous volume flux of surface waters with $\sigma_\theta < 25.0$, ranging from 1.6–5.9 Sv, yields an average volume flux for the 4 months of the SW Monsoon of 0.2–0.7 Sv due solely to this filament. This is a significant fraction of the upwelling volume transport estimated for 1993–1995 by Shi et al. (2000), 1.5 Sv for the entire Oman upwelling zone. This one filament, then, contributes roughly 0.06–0.23 Sv of upwelling to the annual average in the Arabian Sea.

Altimetry suggests that the southern and western limbs of the filament were a distinct anticyclonic mesoscale feature, though the evolution and the importance of its interaction with water in the coastal upwelling region remains unclear. This interaction, however, is indicative of how this coastal upwelling region might be different than the canonical upwelling regions on the eastern boundaries (e.g., California Current system, Peru/Chile, Benguela Current). The EKE in the western part of the Arabian Basin is higher, a result that is general to the world oceans (Stammer and Wunsch, 1999). Eddies then presumably play a larger role where upwelled water ends up and how it disperses than in the eastern upwelling regimes. Many eddy features and thus eddy energy are observed to propagate westward, including the initial propagation of energy away from the California Current system (Kelley et al., 1998; Haney et al., 2001). By contrast, the western boundary in the Oman upwelling regime also may play a role in the eventual fate of upwelled water, though this certainly remains unclear.

At the site of the moored array, the surface heat flux, while small compared to the horizontal heat fluxes, was persistent and positive throughout the year. The cooling horizontal heat flux, including a heat flux in the mixed layer, then is the restoring term that prevents a year-on-year buildup of heat. Climatology shows that the Arabian Sea as a whole gains a large amount of heat over the course of the year, which is compensated generally by upwelling (e.g., Düing and Leetmaa, 1980; Lee and Marotzke, 1998) and a surface heat flux divergence in southward transport. The offshore transport of coastally upwelled water captured by the moored array and SeaSoar survey is then one limb of the meridional overturning circulation of the Indian Ocean, and an important piece of the net poleward transport of heat in the Indian Ocean sector. Although there were not enough measurements to estimate the salinity budget at the moored array, there was generally a strong vertical salinity gradient, with saltier water overlying fresher water, formed from the strong balance towards evaporation over precipitation in the Arabian Sea. In fact, the surface buoyancy flux, which when negative can drive convective entrainment into the mixed layer, has a significant contribution from salinity through the evaporative flux (Weller et al., 2002). The filament brings fresher water, upwelled from depth, to the surface (Fig. 14). In an analog to the heat budget, the freshening provided by this export of coastally upwelled water is a restoring

term that prevents the year-on-year buildup of salinity.

4. Conclusions

An estimation of the terms in the upper-ocean heat budget in the central Arabian Sea using data from a moored array includes not only a direct response to the surface forcing, but strong episodic modulation from mesoscale variability in the horizontal advection, roughly balanced in the temperature trend. This mesoscale modulation took two forms, one in each monsoon season. During the NE Monsoon, the passage of a series of mesoscale eddies with large variations in thermocline depth but a small surface signature was the major contributor to the heat budget. Satellite altimetry and SST imagery revealed that these eddies appeared during the previous SW Monsoon season, and lost much of their surface signature during the Spring Intermonsoon. The estimated horizontal heat flux within the mixed layer was for the most part not significantly different from zero, and the largest horizontal heat fluxes, as well as changes in temperature, came just below the mixed layer, associated with the advection of thermocline 'topography' past the array.

The transport of cool, coastally upwelled water in a filament to the site of the moored array, more than 600 km offshore, was the major contribution to the SW Monsoon upper-ocean heat budget. The altimetric and satellite SST record suggest that this filament was associated with the interaction of the coastal upwelling region and an anticyclonic eddy. A comparison of water mass properties between the moored array and a SeaSoar survey from close to the Omani coast confirms the transport of coastally upwelled water to the site of the moored array.

The inferred vertical velocity required to close the heat budget at the moored array was strong and episodic, typical of vertical circulations associated with the mesoscale, and an order of magnitude larger than an estimate of the vertical velocity due to Ekman pumping. To explain the patterns of cooling and deepening of the mixed layer in the central Arabian Sea during the SW

Monsoon, Lee et al. (2000) found that locally wind-driven entrainment was more important than Ekman pumping, but neither fully explained observed patterns. At the site of the moored array during the SW Monsoon, mixed-layer deepening and cooling were initially locally provoked by entrainment driven by the strong surface winds (Weller et al., 2002). The cooling was then reinforced by offshore horizontal advection of coastally upwelled water, which at the same time reinforced the vertical stratification, bringing the upper thermocline closer to the surface. These mechanisms—wind-driven entrainment, and coastal upwelling and horizontal advection off-shore—are the critical balance that explain the mixed-layer evolution at the site of the moored array, and suggest horizontal advection of coastally upwelled water as an explanation of the shallow mixed layers shoreward of the peak of the Findlater Jet. Further offshore, the mixed layer presumably continues to deepen in response to wind-driven entrainment, less likely to be reached by the same type of coastally-connected horizontal advection. In the basin in general, Ekman pumping likely plays a secondary role in modulating the depth of the thermocline.

Productivity, as measured by chlorophyll *a* concentrations in the SeaSoar survey, and at the moored array (Dickey et al., 1998), was for the most part strongly tied to the mesoscale variability, and is likely affected by the associated secondary vertical circulations or by direct horizontal advection of coastally upwelled water.

The combination of the strong volume flux of the SW Monsoon filament (instantaneous fluxes of 1.6–5.9 Sv for $\sigma_\theta < 25.0$ or 0.2–0.7 Sv averaged over the SW Monsoon), integrated section heat fluxes that are a significant percentage (3–18%) of a previous estimate of the total heat flux due to coastal upwelling (Düing and Leetmaa, 1980), and elevated levels of eddy activity during the SW Monsoon and near the Arabian Peninsula coast (Kim et al., 2001), point to the importance of this mesoscale-modulated heat transport not only on the upper-ocean heat budget as observed at the moored array, but on the general Arabian Sea upper-ocean heat budget. The coastal filament, and its eventual dispersal, is one mechanism that

allows for the incorporation of deeper water upwelled at the coast into the mixed layer and upper ocean well offshore, closing one limb of the Indian Ocean meridional overturning circulation, and helping to balance the net surface heat flux into the Arabian Sea.

Appendix A

EOF filtering methods and uncertainty in the horizontal heat flux

A.1. Method

The moored data contain variability on all spatial and temporal scales, including those unresolved by the array. The data were first filtered using a truncated series of empirical orthogonal functions (EOFs), which extracted the variability that was coherent across the array (Rudnick and Davis, 1988). The EOFs are the ordered series of eigenvectors of the covariance matrix of the measurements. Because of the widely varying vertical spacing between measurements over the four moorings, the covariance matrix was weighted by a representative height, so that in this case the EOFs are the eigenvectors of the weighted covariance (Müller and Siedler, 1992), $\overline{u_i(t)u_j(t)}\sqrt{h_ih_j}$. Here, $u_i(t)$ and $u_j(t)$ are two time-series of temperature or velocity, and h_i and h_j are the representative vertical range associated with each time-series. In this way the average variance over depth was represented in the EOFs, and highly sampled portions of the ocean are not overrepresented.

The first two EOFs in temperature and velocity are shown in Figs. 19 and 20, for each deployment. The first two EOFs in temperature, and the first in velocity, have uniform vertical structure across the array, for both deployments. The first EOFs are associated with between 74% and 90% of the variability, and the spectra of the time-series associated with them are red, with the most energy at the longest captured time-scales. Higher EOFs have increasingly white spectra in their associated time-series. The spatial uniformity across the array in the first two EOFs, taken along with the spatial variability in the few higher EOFs that still retain significant amounts of associated low-frequency time variability, suggests that the array has been scaled to successfully capture a good portion of the horizontal variability at the site.

The first deployment first EOF for temperature (Fig. 19, associated with 79.4% of the variability) emphasizes changes centered around 100 m depth. There is a mild cooling (warming) in near-surface temperatures accompanying the warming (cooling) at depth, though the time-series associated with EOFs 1 and 2—which is associated with 8.0% of the variability and—are nearly out of phase during the time of maximum variability, early in the deployment (October and November and more mildly into December). Taken together, they indicate that the biggest changes in temperature take place below the surface, centered between 50 and 100 m. During the second deployment, the first EOF in temperature (associated with 84% of the variability) is uniform in depth and across the array, with a slight emphasis around 100 m.
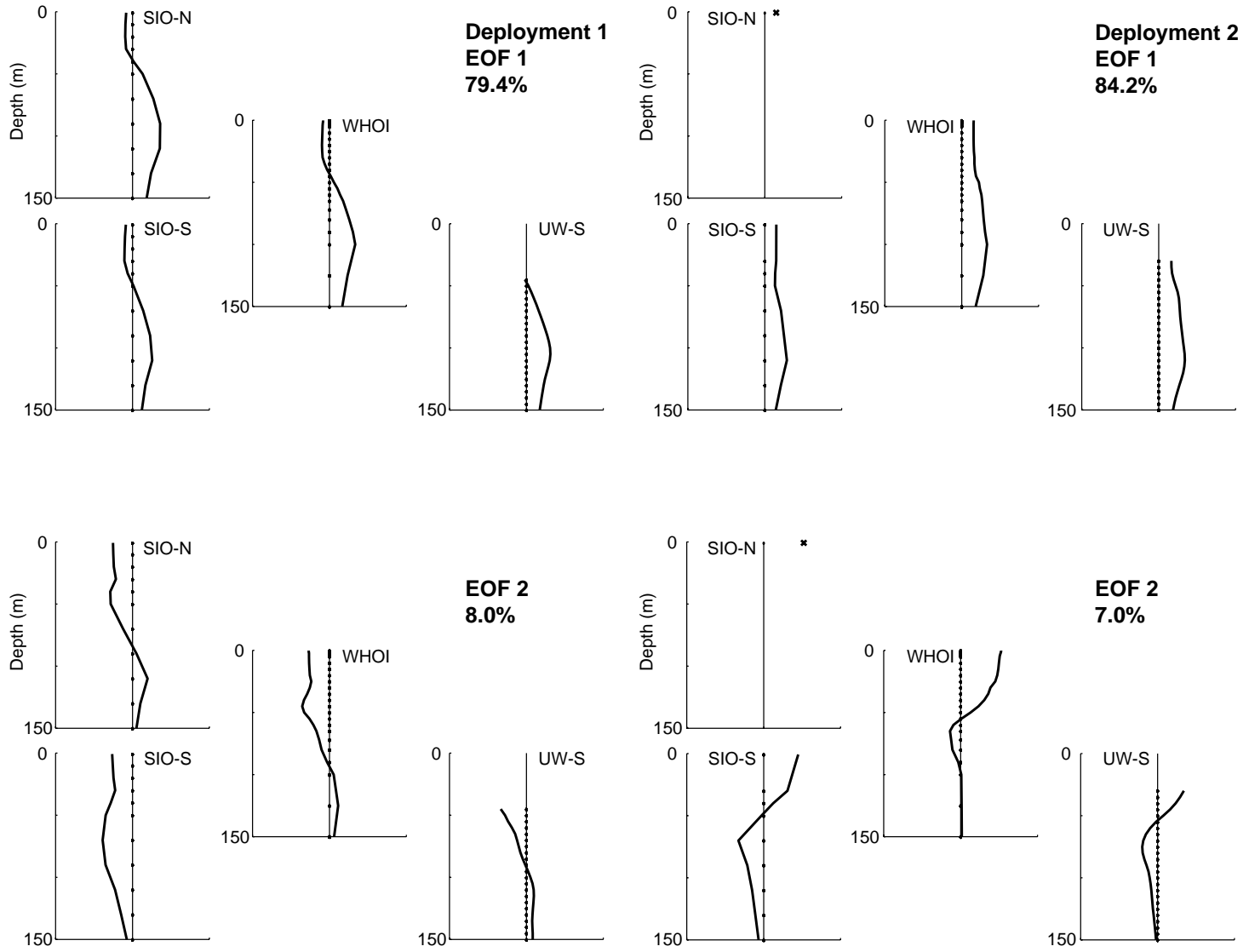
Fig. 19. The first two array EOFs of temperature. For the first deployment (NE Monsoon and Spring Intermonsoon), the largest signal of variability comes in the upper thermocline, just below the mixed layer. During the second deployment (SW Monsoon and Fall Intermonsoon), the largest signal of variability is uniform in sign across all moorings and at all depths, with a slight emphasis around 100 m. Vertical spacing of data indicated by points on the zero axis, and the single surface data point on the SIO-N mooring during the second deployment, included in the EOF, is marked by an 'x'.
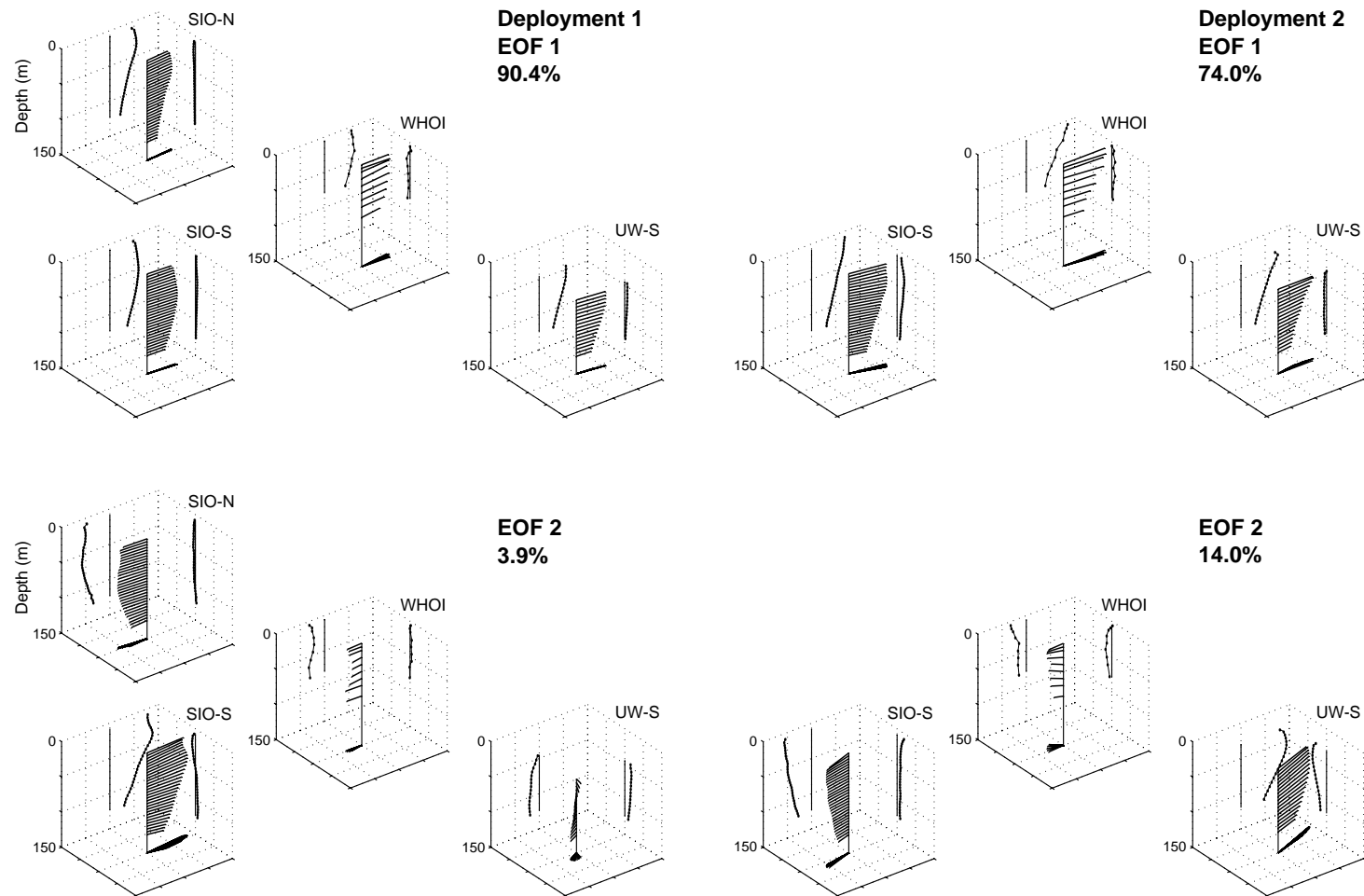
Fig. 20. The first two array EOFs of velocity. For aid in visualization, the tips of the velocity vectors are projected onto the x-, y-, and z- axes on the sides of the box. For the first deployment, the first EOF is quite uniform in direction across the moorings and in depth, while the second EOF is associated with both a north–south velocity shear (with positive vorticity) and a small divergence. For the second deployment, temperature from SIO-N, with a 46% return, was not used, and so the velocity there was not used. As in the first deployment, the first EOF is associated with fairly uniform velocities across the moored array and in depth, although surface intensified. The second EOF is associated with a divergence and a small positive vorticity.

The time-series associated with this EOF suggests that there is a strong change, a cooling, uniform across the array and fairly uniform in depth, starting in the last week of July and lasting through the first two weeks of August. Higher EOFs, associated with less of the total variability, begin to exhibit both higher vertical and greater spatial differentiation across the array.

The first EOFs in velocity for each deployment are uniform in vertical structure across the array, with a surface intensification, and a drop in magnitude from the near-surface high to about half at 100 m (Fig. 20). The strongest variability in these first EOFs is similar to that of the temperature EOFs, strongest in October through December, and in late July and into August.

The temporal mean and the first three or four EOFs of velocity and temperature are retained in the filter as

$$\mathbf{u}(\mathbf{x}_n, t) = \mathbf{u}_0(\mathbf{x}_n) + \sum_{i=1}^{m} \alpha_i(t)\mathbf{u}_i(\mathbf{x}_n),$$

$$T(\mathbf{x}_n, t) = T_0(\mathbf{x}_n) + \sum_{i=1}^{m} \beta_i(t)T_i(\mathbf{x}_n),$$

where $\mathbf{x}_n$ enumerates the instrument position, $\mathbf{u}_0$ and T_0 are the time means, and $\mathbf{u}_i$ and T_i are the EOFs associated with the amplitudes α_i and β_i. The cutoff at $m = 3$ for the first deployment and $m = 4$ for the second deployment was made in each case based on a sharp drop in the remaining

percentage of the variability associated with the EOF (see Fig. 21). Using this type of filtering selectively extracts the variability on the scales that are coherent across the array. The total variance retained by the filtering varied between 92.5% and 96.4%, depending on the deployment and variable.

A.2. Uncertainty

The uncertainty in the estimation of the various terms in the heat budget is important in the understanding of how it closes, and can potentially come from a number of sources: the error in the measurements made by the moored instrumentation, unresolved spatial variability which makes it through the EOF filtering process, and potential mooring line tilt during strong currents, yielding measurements higher (because of the surface-compliant buoyancy in the moorings) in the water column than expected. The UW PCM instrument measured pressure, and so line tilt is not a source of error for this mooring.

The dominant uncertainty in the horizontal heat flux (second term in (1)) comes from the error associated with the spatial filtering. This error can come from large-scale variability that is not retained in the EOF filtering or, more likely, in small-scale variability that is retained. The magnitude of this uncertainty can be estimated from the variance in the first neglected EOF, which is assumed to have (and observed to have) similar
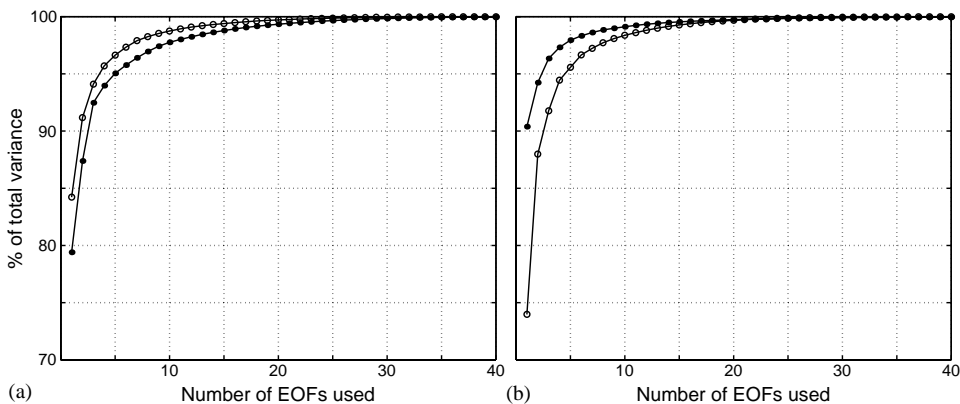

Fig. 21. The EOF variance spectrum for (a) temperature and (b) velocity. Closed dots are for the first deployment, open for the second.

short time-scale variability as the included EOFs. The difference between the horizontal heat flux calculated with unfiltered data and EOF-filtered data is also comparable to the calculated error. The rms error in the temperature from this estimate varies slightly between the two deployments, but is much larger than the instrument error or potential error from mooring tilt, and is $0.25°C$ for the first deployment and $0.18°C$ for the second. The similarly defined rms error in the velocity, at $2.2\,\mathrm{cm\,s^{-1}}$ for the first deployment and $1.8\,\mathrm{cm\,s^{-1}}$ for the second, is likewise much larger than any other sources of uncertainty.

The filtered values of the temperature and velocity at each mooring were spline-fitted (along with their associated error) onto a fixed 5 m resolution grid in the z-direction, providing estimates of the horizontal structure of temperature and velocity at every level. No velocity measurements were made below 80 m on the WHOI mooring, so the estimate of the velocity at the central point of the array is given by the remaining measurements of velocity, and gradients are not computed. The value and $x - y$ gradients of the temperature and each component of the velocity are estimated from the three or four elements at each fixed depth on the grid, using a least squares planar fit. Expressed in the terminology of linear inverse models (Wunsch, 1996),

$$\mathbf{Ex} = \mathbf{y} \quad \text{or} \quad \begin{bmatrix} 1 & x_1 & y_1 \\ & \dots & \\ 1 & x_n & y_n \end{bmatrix} \begin{bmatrix} \bar{u} \\ u_x \\ u_y \end{bmatrix} = \begin{bmatrix} u_1 \\ \dots \\ u_n \end{bmatrix},$$

where $\mathbf{E}$ is the model matrix, containing the positions of the three or four array elements (x_n, y_n) distributed about the central point of the array, $\mathbf{x}$ is the parameter vector containing the mean and x- and y-gradients of the variable (u, representing temperature or one component of velocity), and $\mathbf{y}$ is the data vector, containing the values of the temperature or velocity at each point in the array. Expression in this format allows for an easy estimation of the parameters $\mathbf{x}$ by inversion of the model matrix $\mathbf{E}$. The errors associated with the parameters are also simply expressed as (Wunsch, 1996) $\mathbf{P} = (\mathbf{E}^T\mathbf{E})^{-1}$ $\mathbf{E}^T\mathbf{R}_{nn}\mathbf{E}(\mathbf{E}^T\mathbf{E})^{-1}$, where $\mathbf{R}_{nn}$ is the error covariance

matrix for the data $\mathbf{y}$, estimated as described above. The error associated with the temperature, velocity and gradients is thus readily computed for each fixed depth. As an example, the error associated with the array central point temperature is shown in the right-most panel of Fig. 5. The error varies with deployment and varies in depth, but is generally around $0.1°C$. The estimated horizontal gradients in temperature are above the level of uncertainty for a majority of the time period sampled. There are, however, periods of time when the estimated gradient is not significantly different from zero, the longest of which comes during the NE Monsoon.

The uncertainty in the temperature, velocity, and gradients from the array are propagated into the individual terms of the upper-ocean heat budget ((1) and (2)). The vertical integration of the heat flux terms on the left-hand side of (2) reduces the error by integrating over a number of degrees of freedom. Since the first EOFs in temperature and velocity across the mooring were so dominant, and in large part fairly vertically uniform, the vertical integration is assumed to take place over only four degrees of freedom, represented by each mooring.

The uncertainty in the estimate of the temperature trend term (the first term of (2)), which is calculated as differences in temperature over the time-scale of the sampling, is dependent not on this sampling time-scale, but on the time-scale of variability in the temperature. The temperature trend is coherent over the 4-h time-scale of the measurements, so the error is based on the decorrelation time-scale of the noise, represented by the first ignored EOF. This time-scale is about 40 h, yielding an error in the vertically integrated short-term temperature trend of $180\,\mathrm{W\,m^{-2}}$. The temperature trend term, measuring the change in heat content integrated to a fixed depth, is significantly different from zero for a majority of the observed period.

The uncertainty in the heat advection term (second term in (1) or (2)) is nonlinear, as it is dependent on both the velocity and the gradient in temperature. The uncertainty is largest when the velocities are largest, coincident with the largest horizontal heat fluxes. It is only these large

horizontal heat fluxes that rise above the level of uncertainty, however. Integrated vertically, the uncertainties range from a minimum of 50 to a maximum of $1300\,\mathrm{W\,m^{-2}}$ in the first deployment, and a maximum of $890\,\mathrm{W\,m^{-2}}$ during the second deployment. But the strong horizontal heat fluxes (maximum estimate of about $4500\,\mathrm{W\,m^{-2}}$) are significantly different from zero.

The third term in (2), the vertical advection of heat, is not estimated directly, since no direct measurements of vertical velocity are available. It is estimated as the residual of all the other terms, and so contains the accumulated uncertainty, both explicitly estimated and unaccounted for, from the other terms.

The error in the final term of (2), the net surface heat flux, is estimated to be $15\,\mathrm{W\,m^{-2}}$, and is insignificant compared to both the magnitude of the net surface heat flux and the other uncertainties in the calculation.

References

Bauer, S., Hitchcock, G.L., Olson, D.B., 1991. Influence of monsoonally forced Ekman dynamics upon surface layer depth and plankton biomass distribution in the Arabian Sea. Deep-Sea Research I 38 (5), 531–553.

Brink, K.H., Cowles, T.J., 1991. The coastal transition zone program. Journal of Geophysical Research 96, 14637–14647.

Brink, K., Arnone, R., Coble, P., Flagg, C., Jones, B., Kindle, J., Lee, C., Phinney, D., Wood, M., Yentsch, C., Young, D., 1998. Monsoons boost biological productivity in Arabian Sea. Eos, Transactions, American Geophysical Union 27 (13), 168–169.

Chelton, D.B., Schlax, M.G., 1996. Global observations of oceanic Rossby waves. Science 272, 234–238.

Desai, S.D., Wahr, J.M., 1995. Empirical ocean tide models estimated from TOPEX/Poseidon altimetry. Journal of Geophysical Research 100, 25205–25228.

Dickey, T., Marra, J., Sigurdson, D.E., Weller, R.A., Kinkade, C.S., Zedler, S.E., Wiggert, J.D., Langdon, C., 1998. Seasonal variability of bio-optical and physical properties in the Arabian Sea: October 1994-October 1995. Deep-Sea Research II 45, 2001–2025.

Düing, W., Leetmaa, A., 1980. Arabian Sea cooling: a preliminary heat budget. Journal of Physical Oceanography 10, 307–312.

Feng, M., Hacker, P., Lukas, R., 1998. Upper ocean heat and salt balances in response to a westerly wind burst in the western equatorial Pacific during TOGA COARE. Journal of Geophysical Research 103 (C5), 10289–10311.

Findlater, J., 1969. A major low-level air current near the Indian Ocean during the northern summer. Quarterly Journal of the Royal Meteorological Society 95, 362–380.

Fischer, A.S., 2000. The upper ocean response to the monsoon in the Arabian Sea. Ph.D. Thesis, Massachusetts Institute of Technology and Woods Hole Oceanographic Institution, 00–22, 222pp.

Fischer, J., Schott, F., Stramma, L., 1996. Currents and transports of the Great Whirl-Socotra Gyre system during the summer monsoon, August 1993. Journal of Geophysical Research 101 (C2), 3573–3587.

Flagg, C.N., Kim, H.-S., 1998. Upper ocean currents in the northern Arabian Sea from shipboard ADCP measurements collected during the 1994–1996 US JGOFS and ONR programs. Deep-Sea Research II 45, 1917–1959.

Fox, C.A., 1997. Estimation of mid-latitude Rossby waves using simple ocean model and Kalman filtering with TOPEX/POSEIDON altimeter data. Ph.D. Thesis, University of Colorado, Boulder, CO, 129pp.

Haney, R.L., Hale, R.A., Dietrich, D.E., 2001. Offshore propagation of eddy kinetic energy in the California Current. Journal of Geophysical Research 106 (C6), 11709–11717.

Hastenrath, S., Greischar, L., 1993. The monsoonal heat budget of the hydrosphere–atmosphere system in the Indian Ocean sector. Journal of Geophysical Research 98 (C4), 6869–6881.

Hendricks, J.R., Leben, R.R., Born, G.H., Koblinsky, C.J., 1996. Empirical orthogonal function analysis of global TOPEX/POSEIDON altimeter data and implications for detection of global sea level rise. Journal of Geophysical Research 101 (C6), 14131–14145.

Honjo, S., Dymond, J., Prell, W., Ittekkot, V., 1999. Monsoon-controlled export fluxes to the interior of the Arabian Sea. Deep-Sea Research II 46, 1859–1902.

Kelley, K.A., Beardsley, R.C., Limeburner, R., Brink, K.H., Paduan, J.D., Chereskin, T.K., 1998. Variability of the near-surface eddy kinetic energy in the California Current based on altimetric, drifter, and moored current data. Journal of Geophysical Research 103, 13067–13083.

Kilpatrick, K.A., Podestá, G.P., Evans, R., 2001. Overview of the NOAA/NASA advanced very high resolution radiometer Pathfinder algorithm for sea surface temperature and associated match up database. Journal of Geophysical Research 106 (C5), 9179–9197.

Kim, H.-S., Flagg, C.N., Howden, S.D., 2001. Northern Arabian Sea variability from TOPEX/ Poseidon altimetry data: an extension of the US JGOFS/ONR shipboard ADCP study. Deep-Sea Research II 48, 1069–1096.

Large, W.G., McWilliams, J.C., Doney, S.C., 1994. Oceanic vertical mixing: a review and a model with a nonlocal boundary layer parameterization. Reviews of Geophysics 32 (4), 363–403.

Lee, T., Marotzke, J., 1998. Seasonal cycles of meridional overturning and heat transport of the Indian Ocean. Journal of Physical Oceanography 28, 923–943.

Lee, C.M., Jones, B.H, Brink, K.H., Fischer, A.S., 2000. The upper-ocean response to monsoonal forcing in the Arabian Sea: seasonal and spatial variability. Deep-Sea Research II 47, 1177–1226.

Manghnani, V., Morrison, J.M., Hopkins, T.S., Böhm, E., 1998. Advection of upwelled waters in the form of plumes off Oman during the Southwest Monsoon. Deep-Sea Research II 45, 2027–2052.

McCreary Jr., J.P., Kundu, P., Molinari, R.L., 1993. A numerical investigation of dynamics, thermodynamics, and mixed-layer processes in the Indian Ocean. Progress in Oceanography 31, 181–244.

Mitchum, G.T., 1994. Comparison of TOPEX sea surface heights and tide gauge sea levels. Journal of Geophysical Research 99, 24541–24553.

Molinari, R.L., Olson, D., Reverdin, G., 1990. Surface current distributions in the tropical Indian Ocean derived from compilations of surface buoy trajectories. Journal of Geophysical Research 95, 7217–7238.

Müller, T.J., Siedler, G., 1992. Multi-year current time series in the eastern North Atlantic Ocean. Journal of Marine Research 50, 63–98.

Palmer, T.N., Mansfield, D.A., 1984. Response of two atmospheric general circulation models to sea-surface temperature anomalies in the tropical east and west Pacific. Nature 310, 483–488.

Price, J.F., Mooers, C.N.K., Leer, J.C.V., 1978. Observation and simulation of storm-induced mixed-layer deepening. Journal of Physical Oceanography 8, 582–599.

Price, J.F., Weller, R.A., Pinkel, R., 1986. Diurnal cycling: observations and models of the upper ocean response to diurnal heating, cooling, and wind mixing. Journal of Geophysical Research 91 (C7), 8411–8427.

Rao, K.G., Goswami, B.N., 1988. Interannual variations of sea surface temperature over the Arabian Sea and the Indian monsoon: a new perspective. Monthly Weather Review 116, 558–568.

Rao, R.R., Molinari, R.L., Festa, J.F., 1989. Evolution of the climatological near-surface thermal structure of the tropical Indian Ocean. 1. Description of mean monthly mixed-layer depth, and sea surface temperature, surface current, and surface meteorological fields. Journal of Geophysical Research 94, 10801–10815.

Rudnick, D.L., Davis, R.E., 1988. Mass and heat budgets on the Northern California continental shelf. Journal of Geophysical Research 93 (C11), 14013–14024.

Rudnick, D.L., Weller, R.A., 1993. The heat budget in the North Atlantic subtropical frontal zone. Journal of Geophysical Research 98 (C4), 6883–6893.

Schott, F., 1983. Monsoon response of the Somali Current and associated upwelling. Progress in Oceanography 12, 357–381.

Shearman, R.K., Barth, J.A., Kosro, P.M., 1999. Diagnosis of the three-dimensional circulation associated with mesoscale motion in the California Current. Journal of Physical Oceanography 29, 651–670.

Shi, W., Morrison, J.M., Böhm, E., Manghnani, M., 2000. The Oman upwelling zone during 1993, 1994 and 1995. Deep-Sea Research II 47, 1227–1247.

Shukla, J., 1987. Interannual variability of monsoons. In: Fein, J.S., Stephens, P.L. (Eds.), Monsoons. Wiley, New York, pp. 399–463.

Smith, S.L., Codispoti, L.A., Morrison, J.M., Barber, R.T., 1998. The 1994–1996 Arabian Sea expedition: an integrated, interdisciplinary investigation of the response of the north-western Indian Ocean to monsoonal forcing. Deep-Sea Research II 45, 1905–1915.

Spall, M.A., Weller, R.A., Furey, P.W., 2000. Modelling the three-dimensional upper ocean heat budget and subduction rate during the subduction experiment. Journal of Geophysical Research 105 (C11), 26151–26166.

Stammer, D., Wunsch, C., 1999. Temporal changes in eddy energy of the oceans. Deep-Sea Research II 46, 77–108.

Strub, P.T., Kosro, P.M., Huyer, A., CTZ Collaborators, 1991. The nature of cold filaments in.44 the California Current system. Journal of Geophysical Research 96, 14,743–14,768.

Weller, R.A., Baumgartner, M.F., Josey, S.A., Fischer, A.S., Kindle, J.C., 1998. Atmospheric forcing in the Arabian Sea during 1994–1995: observations and comparisons with climatology and models. Deep Sea Research II 45, 1961–1999.

Weller, R.A., Fischer, A.S., Rudnick, D.L., Eriksen, C.C., Dickey, T.D., Marra, J., Fox, C., Leben, R., 2002. Moored observations of upper-ocean response to the monsoons in the Arabian Sea during 1994–1995. Deep-Sea Research II 49, 2195–2230.

Wunsch, C., 1996. The Ocean Circulation Inverse Problem. Cambridge University Press, Cambridge, UK, 442pp.

Wunsch, C., 1997. The vertical partition of horizontal kinetic energy and the spectrum of global variability. Journal of Physical Oceanography 27, 1770–1794.

Wyrtki, K., 1971. Oceanographic Atlas of the International Indian Ocean Expedition. National Science Foundation Publication OCE/NSF 86-00-001, Washington, DC, 531pp.